Nano Energy 155 (2026) 112038

Contents lists available at ScienceDirect

Nano Energy

journal homepage: www.elsevier.com/locate/nanoen

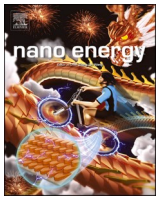

Full paper

High-spin Co sites promote *OOH intermediates generation for H_2O_2 production in sequential dual-cathode electro-fenton processes

Kewang Liu [a,1], Ligang Wang [b,1], Xiaoyu Zhang [a], Haiyin Zhan [a], Huaizhu Wang [c], Weizhao Yan [c], Limin Shen [c], Pengfei Wang [a,*], Zhong Jin [c,*], Sihui Zhan [d,*]

[a] MOE Key Laboratory of Pollution Processes and Environmental Criteria/Tianjin Key Laboratory of Environmental Remediation and Pollution Control, College of Environmental Science and Engineering, Nankai University, Tianjin 300350, PR China
[b] Institute of Molecular Plus, Tianjin University, Tianjin 300072, PR China
[c] State Key Laboratory of Coordination Chemistry, MOE Key Laboratory of Mesoscopic Chemistry, MOE Key Laboratory of High-Performance Polymer Materials and Technology, Jiangsu Key Laboratory of Clean Energy Catalysis and Intelligent Green Chemical Engineering, Suzhou Key Laboratory of Green Intelligent Manufacturing of New Energy Materials and Devices, Tianchang New Materials and Energy Technologies Research Center, Institute of Green Chemistry and Engineering, School of Chemistry and Chemical Engineering, Nanjing University, Nanjing, Jiangsu 210023, PR China
[d] School of Environmental Science and Engineering, Tianjin University, Tianjin 300072, PR China

ARTICLE INFO

Keywords:
Electrocatalysis
Spin state
2e⁻ ORR
*OOH generation
Electro-Fenton

ABSTRACT

Electro-Fenton (EF) is an economical and environmentally friendly wastewater treatment technology, yet its efficiency is often limited by the strong adsorption of the key *OOH intermediate during the two-electron oxygen reduction reaction (2e^- ORR) for H_2O_2 production. Here, we propose a strategy for regulating the spin-state of isolated cobalt sites *via* S coordination (Co_1-NSC). The introduction of S induces the transition of spin-polarization configuration into a high-spin state ($t_{2g}^5 e_g^2$), which optimizes *OOH adsorption strength and enhances H_2O_2 production. The high-spin Co_1-NSC catalyst achieves a H_2O_2 selectivity of 92.3%, and a H_2O_2 production rate of 5.56 mol g_{cat}^{-1} h^{-1} in the flow cell. Additionally, a sequential dual-cathode EF system employing Co_1-NSC as the ORR cathode achieves outstanding Bisphenol A (BPA) removal efficiency (~98% in 60 min) with low energy consumption (0.185 kWh m^{-3}). Experimental and theoretical analyses reveal that sulfur incorporation increases the number of unpaired electrons in the Co 3d orbitals, elevates the spin state of Co sites, and downshifts the d-band center, thereby suppressing *OOH dissociation. This study provides a novel approach for rationally designing 2e^- ORR catalysts through spin regulation, laying the foundation for developing green and sustainable wastewater oxidation treatment technologies.

1. Introduction

Driven by rapid global population growth and industrialization, vast quantities of synthetic chemicals (approximately 300 million tons annually) are produced and utilized [1]. While these synthetic chemicals have undoubtedly contributed positively to human well-being, their residues in water bodies can constitute emerging contaminants (ECs) if they are not effectively degraded [2,3]. Even at very low concentrations (ng L^{-1} to μg L^{-1}), they can pose a threat to the environment and human health [4]. Treatment technologies for ECs can be broadly divided into two main categories: traditional and advanced treatment processes [5]. Traditional treatment technologies primarily include membrane filtration, activated carbon adsorption, and ozone oxidation processes [6]. While these processes have shown some efficacy in treating ECs, most traditional treatment technologies have suboptimal removal efficiency for ECs. This limitation stems from the complex structure of ECs, their poor biodegradability, and their low concentration in water bodies [7,8]. Furthermore, there is the issue of secondary pollution caused by oxidation byproducts in water bodies [9]. Advanced treatment technologies primarily encompass advanced oxidation processes (AOPs), constructed wetlands, and enzymatic treatment [10]. Owing to their ability to non-selectively degrade pollutants, AOPs have emerged as the most extensively researched advanced method for removing ECs from water [11]. Among AOPs, those based on hydrogen peroxide (H_2O_2) are particularly prominent, as they generate highly oxidative radicals (e.g., ·OH) alongside environmentally benign byproducts (H_2O, O_2), leading

* Corresponding authors.
E-mail addresses: pengfeiwang@nankai.edu.cn (P. Wang), zhongjin@nju.edu.cn (Z. Jin), shzhan@tju.edu.cn (S. Zhan).
[1] Kewang Liu and Ligang Wang contributed equally.

https://doi.org/10.1016/j.nanoen.2026.112038
Received 12 January 2026; Received in revised form 28 April 2026; Accepted 17 May 2026
Available online 25 May 2026

to their widespread application in ECs remediation [12–14].

Traditional H_2O_2-based AOPs, such as the homogeneous Fenton process, suffers from inherent limitations, including iron sludge accumulation, difficult catalyst recovery and a narrow applicable pH range [15–17]. Furthermore, the synthesis of industrial H_2O_2 used in the homogeneous Fenton process involves an energy-intensive anthraquinone oxidation process. The high-concentration H_2O_2 produced by it often comes with issues such as high transportation costs and significant hazards when used downstream [18,19]. Consequently, the electro-Fenton (EF) process is gaining increasing prominence in the treatment of ECs for its advantage to generate and activate H_2O_2 [20–24]. In the EF systems, H_2O_2 can be continuously generated *in situ via* two electron oxygen reduction reaction ($2e^-$ ORR) (Eq. 1) under aerobic conditions. Then, H_2O_2 is subsequently activated by Fe(II) or *via* direct electron transfer to generate potent reactive oxygen species (ROS), including hydroxyl radicals (·OH) (Eqs. 2 and 3), superoxide radicals ($O_2^{\cdot-}$), and singlet oxygen ($^1O_2$) [25–27].

$$O_2 + 2H^+ + 2e^- \rightarrow H_2O_2 \quad (1)$$

$$Fe(II) + H_2O_2 \rightarrow Fe(III) + OH^- + \cdot OH \quad (2)$$

$$H_2O_2 + e^- \rightarrow \cdot OH + OH^- \quad (3)$$

However, the lack of highly selective and active $2e^-$ ORR catalysts limit the efficiency of *in situ* H_2O_2 synthesis. The efficiency of H_2O_2 generation directly determines the number of reactive radicals produced, which in turn determines the ability of EF to degrade organic pollutants. Carbon-based single atom catalysts (SACs) have been shown to have excellent $2e^-$ ORR performance [28–30]. But they still suffer from unstable catalytic activity due to low metal-atom loading and the propensity for undesired H_2O_2 reduction reactions (H_2O_2RR) to occur [31–33]. The electronic spin state can reflect the electronic structure and control the catalytic performance of the catalyst [34,35]. Studies have demonstrated that adjusting the spin state of metal active sites can directly influence the d-band centers and charge transport, thereby regulating the adsorption/desorption strength of oxygen intermediates (*OOH and *O) during the oxygen reduction reaction (ORR) [36]. Notably, introducing elements with strong electron-donating ability and weak coordination field splitting energy (such as S) significantly enhances the spin state of active sites. Active sites with high spin states exhibit weaker adsorption of oxides, promoting *OOH desorption. Although spin modulation *via* heteroatom coordination doping has been extensively studied to enhance catalytic performance in fields such as ORR and CO_2 reduction reaction (CO_2RR) [37,38], it has not been extended to the EF processes for achieving highly selective and active *in situ* H_2O_2 generation. This work presents a preliminary attempt to employ a spin-modulation strategy to suppresses the dissociation of the *OOH intermediate, enabling efficient H_2O_2 synthesis in a sequential dual-cathode EF system.

Herein, we propose a strategy to modulate the spin-state of isolated cobalt sites *via* sulfur coordination (Co_1-NSC). Experimental results demonstrate that S atom incorporation reduces the spin-orbit splitting (ΔE) of Co sites, resulting in a high-spin configuration ($t_{2g}^5 e_g^2$). Notably, Co_1-NSC with high-spin Co sites exhibits outstanding performance in the $2e^-$ ORR, achieving 92.3% H_2O_2 selectivity. In a flow cell, a bulk H_2O_2 production rate of 5.56 mol g_{cat}^{-1} h^{-1} was achieved, with a corresponding Faradaic efficiency (FE) of ~90%. Furthermore, a sequential dual-cathode EF system employing Co_1-NSC as the catalyst for *in situ* H_2O_2 synthesis achieved nearly 98% Bisphenol A (BPA) removal efficiency within 60 min using only oxygen as the feedstock. The degradation pseudo-first-order reaction rate of this system is 3.6 times that of the Co_1-NC cathode system, with a lower treatment energy consumption (0.185 kWh m^{-3}) compared to conventional methods. *In-situ* Raman spectroscopy, *in-situ* attenuated total reflectance surface-enhanced infrared absorption spectroscopy (ATR-SEIRAS) and theoretical analysis indicate that S introduction increases the number of unpaired electrons in cobalt 3d orbitals, elevates the spin state of cobalt sites, and shifts the d orbital center downward. This suppresses *OOH decomposition while promoting H_2O_2 generation.

2. Results and discussion

To integrate sulfur from the polysaccharide matrix and nitrogen from urea, a sol-gel method was applied using carrageenan-derived hydrogels. The resulting hydrogel was pyrolyzed to afford a cobalt single-atom catalyst anchored on N, S co-doped carbon (Co_1-NSC) (Fig. 1a). For comparison, bare NSC without added Co precursor and Co_1-NC without sulfur doping were also prepared. Over the carbonization process, the hydrogel was converted into porous carbon with a pore size of 400–500 nm (Fig. S1), which led to an impressive specific surface area of 1296 m^2 g^{-1} and an abundant porosity structure (Fig. S2). X-ray diffraction (XRD) analysis indicates that the prepared materials exhibit characteristic peaks corresponding to the (002) and (101) crystal planes of graphitic carbon (Fig. S3). Notably, no peaks associated with crystalline Co were detected, indicating preliminary evidence of Co dispersion on the carbon substrate. Furthermore, transmission electron microscopy (TEM) images also reveal that no discernible metal crystals present (Fig. 1b, Fig. S4). In addition, Raman spectroscopy shows that the prepared materials have characteristic peaks of disordered D bands (I_D) at 1340 cm^{-1} and ordered graphite carbon G bands (I_G) at 1590 cm^{-1}, and the I_D:I_G values greater than 1.0, indicating a high defect density of the material (Fig. S5). These results clearly indicate that hydrogels undergo high-temperature pyrolysis to form amorphous graphite carbon scaffolds, whose large specific surface area and high defect density will promote improved catalytic performance.

Inductively coupled plasma mass spectrometry (ICP-MS) was used to analyze the Co atom content in the materials, and the results show that the Co loading in Co_1-NSC and Co_1-NC is 0.88 wt% and 0.93 wt%, respectively, demonstrating similar metal loading in two materials (Fig. S6, Table S1). Energy dispersive X-ray spectroscopy (EDS) elemental mapping analysis revealed the coexistence of C, N, S, and Co, which are uniformly distributed (Fig. S7). Metal atoms (white circles) were identified as being atomically dispersed on the Co_1-NSC scaffold by the high-angle annular dark-field scanning TEM (HAADF-STEM) measurements (Fig. 1c). X-ray photoelectron spectroscopy (XPS) shows that Co_1-NSC mainly contains Co, O, N, C, and S elements (Fig. S8a). The high-resolution N 1 s XPS spectra of Co_1-NSC shows five peaks at binding energies of 398.1, 399.2, 399.9, 400.8, and 401.7 eV, corresponding to pyridinc N, Co-N, pyrrolic N, graphite N, and oxidized N, respectively (Fig. S8b). The high-resolution S 2p XPS spectrum of Co_1-NSC can be decomposed into C-SO_x (168.7 eV), S $2p_{1/2}$ (164.7 eV), and S $2p_{3/2}$ (163.4 eV). Notably, the presence of a peak at 162.3 eV, attributing to the Co-S bond, indicates a first-shell coordination structure between S and Co atoms (Fig. S8c) [39]. The survey spectrum of Co_1-NC indicates the presence of Co, O, N, and C. No distinct S characteristic peaks were observed (Fig. S9a). In addition, similar to Co_1-NSC, the high-resolution N 1 s XPS spectrum of Co_1-NC can also be decoupled into five characteristic peaks, corresponding to pyridine N (396.4 eV), Co-N (397.5 eV), pyrrolic N (399.3 eV), graphite N (400.5 eV), and oxidized N (404.6 eV) (Fig. S9b). The high-resolution S 2p XPS spectrum of NSC can be resolved into three peaks, corresponding to S $2p_{3/2}$ (163.5 eV), S $2p_{1/2}$ (164.6 eV), and C-SO_x (168.1 eV) (Fig. S10). It is worth noting that, since no Co precursor was added, no characteristic peaks for Co-N or Co-S are observed.

X-ray absorption near-edge structure (XANES) analysis was employed to further elucidate the chemical state and local coordination environment of Co atoms. The Co *K*-edge XANES spectra reveal that the absorption edge position of Co_1-NSC lies between those of Co foil and CoO, and is closer to CoO, indicating a Co valence state near + 2 (Fig. 1d). Furthermore, the k^3-weighted Fourier transform (FT) of the extended X-ray absorption fine structure (EXAFS) spectra for both Co_1-NSC and Co_1-NC (Fig. 1e) exhibit a single dominant peak at

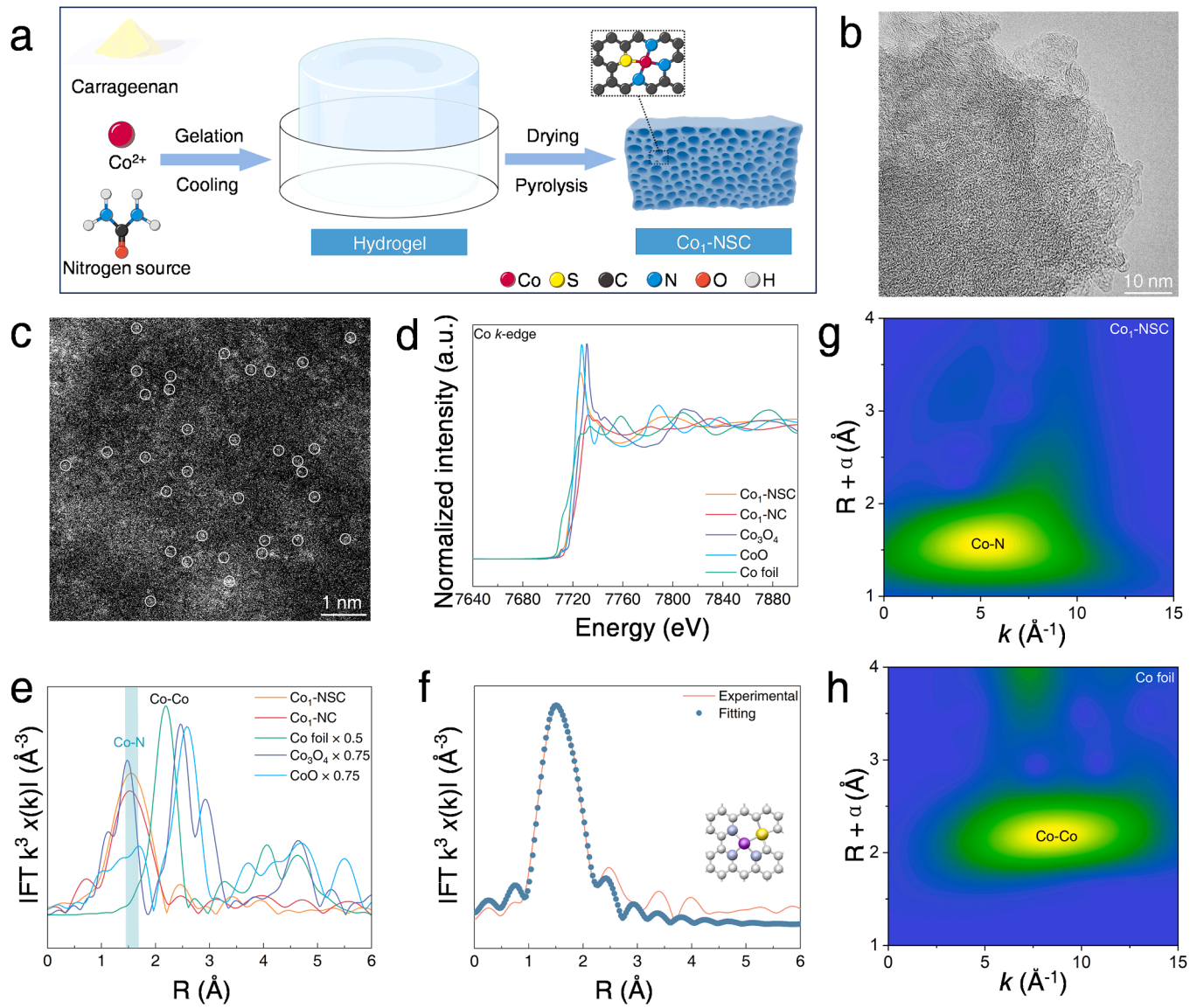

Fig. 1. Synthesis and Characterization of Co_1-NSC. (a) Schematic diagram of the Co_1-NSC preparation process. (b) TEM and (c) HAADF-STEM images of Co_1-NSC. (d) Co K-edge XANES spectra. (e) k^3-weighted FT spectra in R-space. (f) Fitting of the EXAFS spectra of Co_1-NSC in the R space. The inset shows the schematic diagram of the Co_1-NSC structure. WT-transform of (g) Co_1-NSC and (h) Co foil.

approximately 1.5 Å in the first coordination shell. This peak is attributed to backscattering interactions between Co and low-Z atoms such as C, N, and S. Notably, neither Co_1-NSC nor Co_1-N C exhibits a Co-Co scattering path at 2.2 Å, indicating that the Co atoms in both materials are isolated single atoms dispersed on an N/S-doped carbon matrix, consistent with HAADF-STEM results. Fitting results in R space show that Co atoms in Co_1-NSC coordinate with three N atoms and one S atom (Fig. 1f, Fig. S11, Table S2). In Co_1-NC, Co atoms are coordinated with four N atoms (Fig. S12a, Table S2). Wavelet transform (WT) analysis of the k^3-weighted EXAFS spectrum shows that the WT maxima of Co_1-NSC and Co_1-NC are both around 5.5 $Å^{-1}$, significantly different from the WT maximum of the Co foil (8.1 $Å^{-1}$), confirming the absence of Co clusters (Fig. 1g, h, and Fig. S12b).

Recent reports indicate that the electronic structure of Co atoms changes depending on their coordination environment, leading to changes in their spin state. For example, the electronic configurations of the low-spin state (LS) and high-spin state (HS) of Co (III) are $t_{2g}^6e_g^0$ and $t_{2g}^4e_g^2$, respectively, while those of Co (II) are $t_{2g}^6e_g^1$ and $t_{2g}^5e_g^2$, respectively (Fig. 2a). Spin-orbit splitting (ΔE) is closely related to the spin state of transition metal atoms. Crystal field theory indicates that a larger ΔE favors electron pairing, thereby stabilizing lower spin states. Conversely, a smaller ΔE reduces the tendency for electron pairing, promoting higher spin states [40]. ΔE can be expressed as the energy difference between $Co2p_{1/2}$ and $Co2p_{3/2}$ [34]. As shown in Fig. 2b, compared to $\Delta E_{Co1\text{-}NC}$ (15.4 eV), the smaller $\Delta E_{Co1\text{-}NSC}$ (15.0 eV) suggests that the Co species in Co_1-NSC may exhibit a higher spin state than those in Co_1-NC. This result preliminarily indicates that S stoms incorporation modulates the electronic structure and spin state of the Co center. The temperature dependence of the magnetic susceptibility further confirms the high spin state of Co in Co_1-NSC (Fig. 2c). According to the modified Curie-Weiss law, the effective magnetic moment (μ_{eff}) of Co_1-NSC can be calculated to be 3.25 μ_B. Compared with Co_1-NC, Co_1-NSC exhibits a higher spin magnetic moment, suggesting that the 3d orbitals of its Co atoms may contain more unpaired electrons [41]. Furthermore, based on the relationship between μ_{eff} and the spin state, the spin state of the cobalt center in Co_1-NSC can be calculated as 14.4% LS and 85.6% HS. The results of the electron paramagnetic resonance (EPR) spectrum analysis are shown in Fig. 2d. The EPR peak intensity of Co_1-NSC is higher than that of Co_1-NC, suggesting that its Co-3d orbitals contain more unpaired electrons. The above results

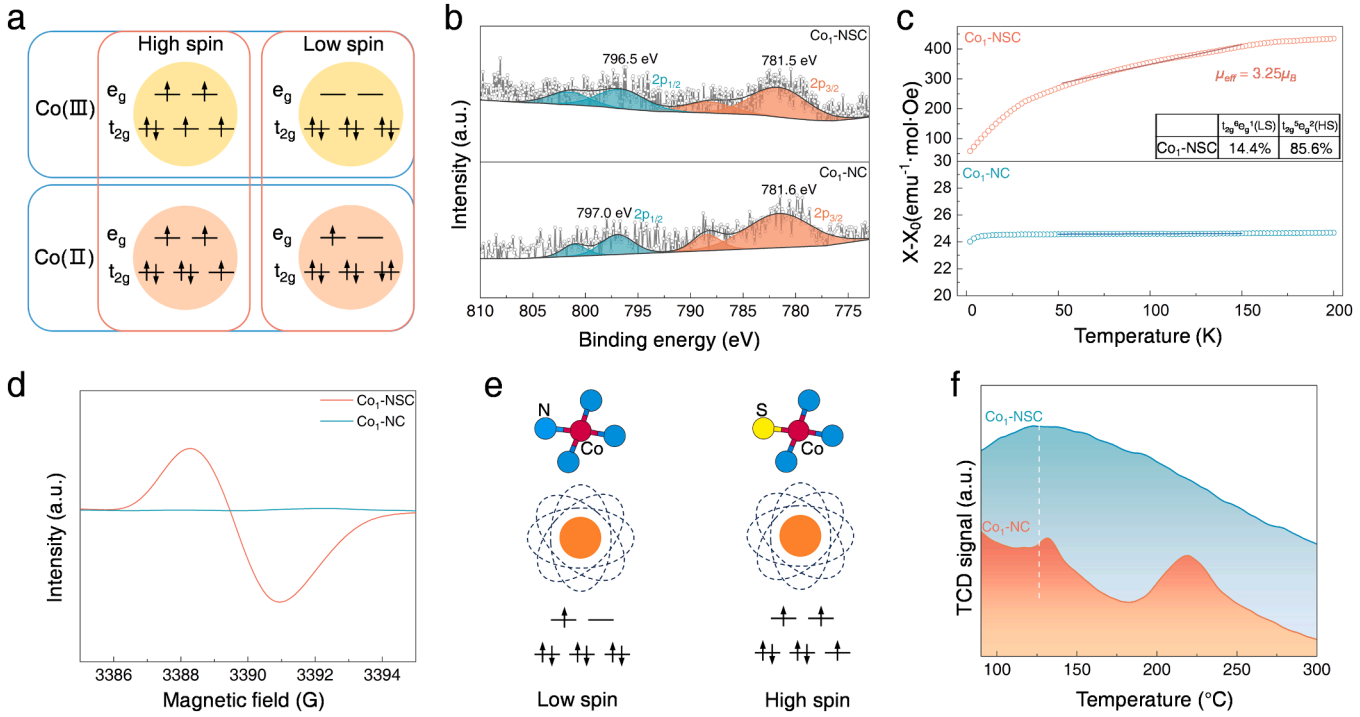

Fig. 2. Analysis of the Co atomic spin state. (a) Schematic diagram of Co (II) and Co (III) spin states. (b) XPS spectra of Co 2p for Co_1-NSC and Co_1-NC. (c) Fitted susceptibility vs temperature based on Curie-Weiss law for Co_1-NSC and Co_1-NC. (d) EPR spectra for Co_1-NSC and Co_1-NC. (e) Schematic diagram of the spin states of Co atoms in Co_1-NSC and Co_1-NC. (f) O_2-TPD curves Co_1-NSC and Co_1-NC.

indicate that the Co atoms in Co_1-NSC are in the high-spin state, with an electronic configuration of $t_{2g}^5e_g^2$, while Co_1-NC is in the low-spin state with an electronic configuration of $t_{2g}^6e_g^1$ (Fig. 2e). Studies have shown that high-spin metal atoms exhibit weaker adsorptive strength towards oxygen-containing compounds compared to those in a low-spin state [42–44]. This difference is also confirmed by O_2 temperature-programmed desorption (O_2-TPD) analysis (Fig. 2f, Fig. S13). The O_2-TPD profile reveals that the signal intensity of Co_1-NSC is significantly higher than that of Co_1-NC, with a lower desorption temperature. This may be due to the fact that high-spin configurations have more unpaired electrons in the Co 3d orbitals; these unpaired electrons act as additional orbitals capable of coordinating with O_2 molecules, thereby enhancing the catalyst surface's ability to adsorb O_2 [45]. This difference in oxygen adsorption indicates that fewer O_2 molecules adsorb on the active sites of Co_1-NC, and the binding strength between O_2 molecules and these sites is stronger. Consequently, O_2 struggles to further form *OOH and desorb, leading to the formation of the $4e^-$ ORR pathway. In contrast, Co_1-NSC exhibits higher reactivity toward O_2, but with weaker binding strength, which may favor *OOH formation and efficient desorption, demonstrating high selectivity toward H_2O_2 [46,47]. Overall, the incorporation of S into the Co-N_4 coordination environment modifies the local crystal field, reduces the spin-orbit splitting ΔE, and increases the fraction of high-spin Co centers. This spin-state modulation is expected to weaken the adsorption of oxygen-containing intermediate species on Co sites.

The rotating ring-disk electrode (RRDE) (Fig. S14) was used to evaluate the $2e^-$ ORR performance of the catalyst in 0.05 H_2SO_4 solution. When switching from N_2 to O_2, a distinct cathodic peak appeared in the cyclic voltammetry (CV) curves (Fig. S15), indicating the presence of a potential-driven oxygen reduction process on the Co_1-NSC surface. This was further confirmed by measurements of the linear sweep voltammetry (LSV) (Fig. 3a). The LSV curve includes the ORR current density recorded on the disk electrode (J_d, solid line, mA cm^{-2}) and the H_2O_2 oxidation current recorded on the platinum ring electrode (J_r, dashed line, mA cm^{-2}). Among the three samples, Co_1-NSC has the highest onset potential (E_{onset}) of 0.703 V *vs*. RHE (Fig. S16a). Notably, the half-wave potential of Co_1-NC is slightly higher than that of Co_1-NSC (Fig. S16b). However, the kinetic current density for H_2O_2 generation (J_k) calculated using the Koutchek-Levy equation indicates that Co_1-NC has the lowest J_k among the three samples (Fig. S16c), further confirming that its Co sites possess stronger binding affinity for O_2, leading to reduced H_2O_2 selectivity. In addition, we calculated the H_2O_2 selectivity (H_2O_2 %) and the number of electron transfers (n) for these three sets of samples based on I_d (mA) and I_r (mA) (Fig. 3b). Over a wide potential range of 0.1–0.7 V *vs*. RHE, Co_1-NSC maintained higher H_2O_2 % and lower n values compared to NSC and Co_1-NC. Specifically, Co_1-NSC exhibited the highest H_2O_2 % (92.3%) and the lowest n value (2.15) at a potential of 0.65 V *vs*. RHE, significantly outperforming the values calculated for Co_1-NC (28.2% and 3.44) and NSC (13.1% and 3.74) at this potential (Fig. 3c), This indicates that the ORR occurring at the active sites of Co_1-NSC is closer to the $2e^-$ ORR. *In-situ* Raman spectroscopy further revealed the differences in the evolution of oxygen-containing intermediate species between the two materials. As shown in Fig. 3d, *in situ* Raman spectroscopy detected a peak at 1520 cm^{-1}, which was attributed to adsorbed *OOH [48,49]. However, no peak at 1520 cm^{-1} was detected on the Co_1-NC surface, indicating that Co_1-NSC promotes the formation of *OOH, thereby exhibiting higher H_2O_2 selectivity. In addition, Co_1-NSC exhibits a significantly smaller Tafel slope (241.8 mV dec^{-1}), indicating faster reaction kinetics (Fig. S16d). Co_1-NSC has a larger electrochemical active surface area (ECSA), which is conducive to charge transfer during the catalytic process (Fig. S17). The above results indicate that O_2 adsorbed on Co_1-NSC is more readily converted to *OOH, which favors the subsequent formation of H_2O_2. We further investigated the effect of different S contents on the $2e^-$ ORR performance of the catalyst (Fig. S18a). As shown in Fig. S18b, the J_r and J_d values were significantly reduced in the sample containing 2 g of i-carrageenan, whereas these values were relatively similar in the samples containing 4 g and 5 g of i-carrageenan. Furthermore, the calculated H_2O_2 % and n values for the sample containing 5 g of i-carrageenan did not differ significantly from those of the sample containing 4 g of

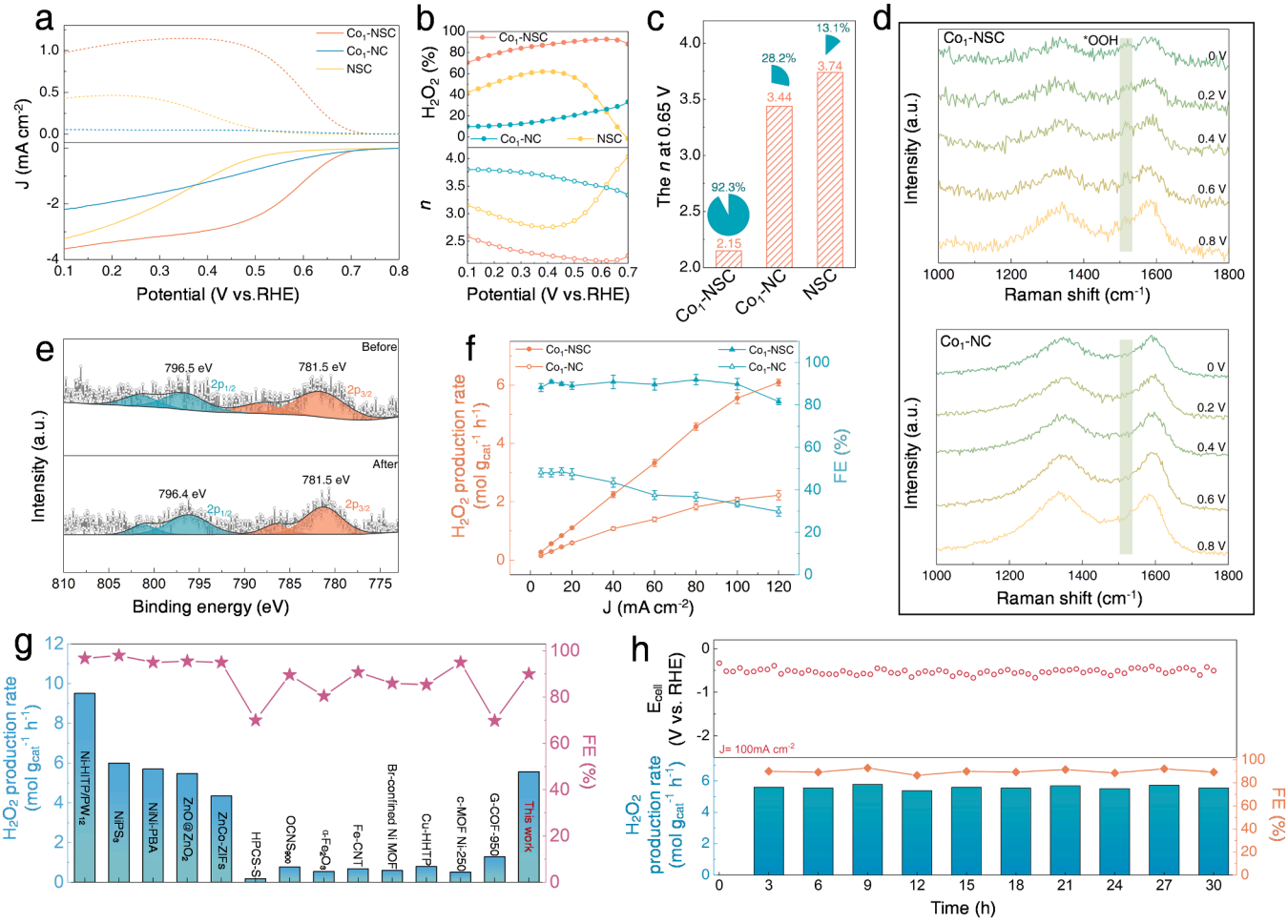

Fig. 3. Electrocatalytic ORR performance. (a) LSV curves recorded in 0.05 H_2SO_4 saturated with O_2, showing the disk current (solid line) and ring current (dashed line). (b) Calculated H_2O_2 selectivity and *n* as a function of applied potential. (c) The highest H_2O_2 selectivity and n exhibited by the three samples. (d) *In-situ* Raman spectrum for Co_1-NSC and Co_1-NC. (e) The high-resolution Co 2p XPS spectra before and after stability test in H-type cell. (f) H_2O_2 production rate and FE of Co_1-NSC and Co_1-NC in Flow cell. (g) Comparison of the FE and production rate of Co_1-NSC and other recently reported electrocatalysts. (h) Long-term stability test of Co_1-NSC in flow cell.

i-carrageenan (Fig. S18c). These results indicate that the sample prepared using 4 g of i-carrageenan already exhibits excellent $2e^-$ ORR performance, and further increasing the sulfur content does not significantly improve the $2e^-$ ORR performance of this material.

To identify the catalytic center, thiocyanate ions (SCN^-) were added to the electrolyte as metal ion inhibitors. As shown in Fig. S19, the current density of Co_1-NSC decreased. Subsequently, after the sample was cleaned and run in a new electrolyte, the LSV curve returned to normal. This experimental result indicates that a metal-based catalytic process exists on Co_1-NSC, with Co sites serving as the primary catalytic active centers. In addition, we calculated the adsorption free energies of O_2 molecules at the Co and S sites on Co_1-NSC and at the Co sites on Co_1-NC. As shown in Fig. S20 and Table S3, the adsorption free energy of the O_2 molecule at the Co site in Co_1-NSC is the lowest, at −0.808 eV, which is significantly lower than that at the Co site in Co_1-NC (-0.554 eV). This indicates that O_2 is more likely to adsorb on high-spin Co sites with more 3d electrons, which is consistent with the O_2-TPD results. It is worth noting that the adsorption free energy of O_2 molecules at the S site of Co_1-NSC is 0.618 eV, indicating that the adsorption of O_2 at the S site is thermodynamically unfavorable; O_2 molecules will not spontaneously and stably adsorb at this site, which further confirms that the Co site is the actual active site on Co_1-NSC.

The performance of the synthesized samples in bulk synthesis of H_2O_2 was tested using a three-electrode H-type cell which consists of a cathode chamber and an anode chamber, separated by a proton exchange membrane (PEM) (Fig. S21). The sample was loaded onto hydrophobic carbon fiber fabric (CFF) and placed as the working electrode in the cathode chamber, where it was electrolyzed for 1 h at a constant potential. The accumulation of H_2O_2 in the electrolyte of the cathode chamber was determined using the Ce^{4+}/Ce^{3+} titration method (Fig. S22). The LSV curve shows that Co_1-NSC has a higher current density under the same constant applied voltage. In addition, the current density of bare CFF is extremely low, and its contribution to H_2O_2 yield and Faradaic efficiency (FE) can be neglected Fig. S23). As shown in Fig. S24a, within the potential range of 0.1–0.5 V *vs.* RHE, the electrolytic H_2O_2 yield and FE of Co_1-NSC were superior to those of Co_1-NC. Notably, Co_1-NSC achieved a yield of 1507 mmol g_{cat}^{-1} h^{-1} and a FE of ~91% at a potential of 0.2 V *vs.* RHE. The stability of Co_1-NSC in H-type cell was determined at a fixed operating voltage of 0.2 V *vs.* RHE (Fig. S24b). The ORR current and H_2O_2 synthesis capacity remained stable over 10 synthesis cycles, with a current intensity decrease of only 4.4%, indicating its potential as a practical $2e^-$ ORR catalyst. High-resolution Co 2p XPS spectra obtained after stability testing shows that the chemical state of the Co sites in Co_1-NSC remains stable after 10 cycles of cyclic ORR testing, remaining a small ΔE (14.9 eV), indicating the stability of its spin state (Fig. 3e). Additionally, TEM images and XRD spectra further confirm the structural stability of the Co_1-NSC catalyst (Fig. S25).

To further investigate the performance of Co_1-NSC in the electrochemical synthesis of H_2O_2 at high current densities, we used a gas diffusion electrode (GDE) to further evaluate the H_2O_2 production rate and FE of Co_1-NSC. As expected, compared to the H-type cell, the corresponding current of Co_1-NSC increased significantly within the same applied potential range when using a GDE (Fig. S26). As shown in Fig. 3f, Co_1-NSC maintained a FE of ~90% over the current density range of 5–100 mA cm^{-2}, whereas Co_1-NC exhibited a maximum FE of only 48.7%. Furthermore, at a current density of 100 mA cm^{-2}, the H_2O_2 production rate of Co_1-NSC reached 5.56 mol g_{cat}^{-1} h^{-1}, significantly higher than that of Co_1-NC (2.07 mol g_{cat}^{-1} h^{-1}). This measured H_2O_2 production rate and FE outperform most recently reported 2e^- ORR electrocatalysts (Fig. 3g and Table S4) [50–62]. It is worth noting that when the applied current density was increased to 120 mA cm^{-2}, the FE of Co_1-NSC showed a significant decrease, which may be attributed to the reduction and/or decomposition of H_2O_2. Subsequently, we tested the stability of Co_1-NSC for the electrochemical synthesis of H_2O_2 at an applied current density of 100 mA cm^{-2}. As shown in Fig. 3h, during the 30 h electrolysis experiment, the cell voltage (E_{cell}) stabilized at approximately 0.5 V *vs.* RHE. Furthermore, neither the H_2O_2 production rate nor the FE showed any significant decline. These results demonstrate that Co_1-NSC exhibits excellent H_2O_2 electro-synthesis performance and long-term stability under high current densities.

To better elucidate the reasons behind the outstanding 2e^- ORR performance of Co_1-NSC, density functional theory (DFT) calculations were further conducted to investigate the thermodynamic processes of the reaction. The optimized material structure model is depicted in Fig. S27. At the equilibrium potential (U = 0.7 V *vs.* RHE), the adsorption of *OOH on an ideal 2e^- ORR catalyst should be thermodynamically neutral, corresponding to ΔG*OOH ~ 3.5 eV. As shown in Fig. 4a, Co_1-NSC (0.20 eV) exhibits a lower overpotential for H_2O_2 production compared to Co_1-NC (0.36 eV), indicating its superior activity for H_2O_2

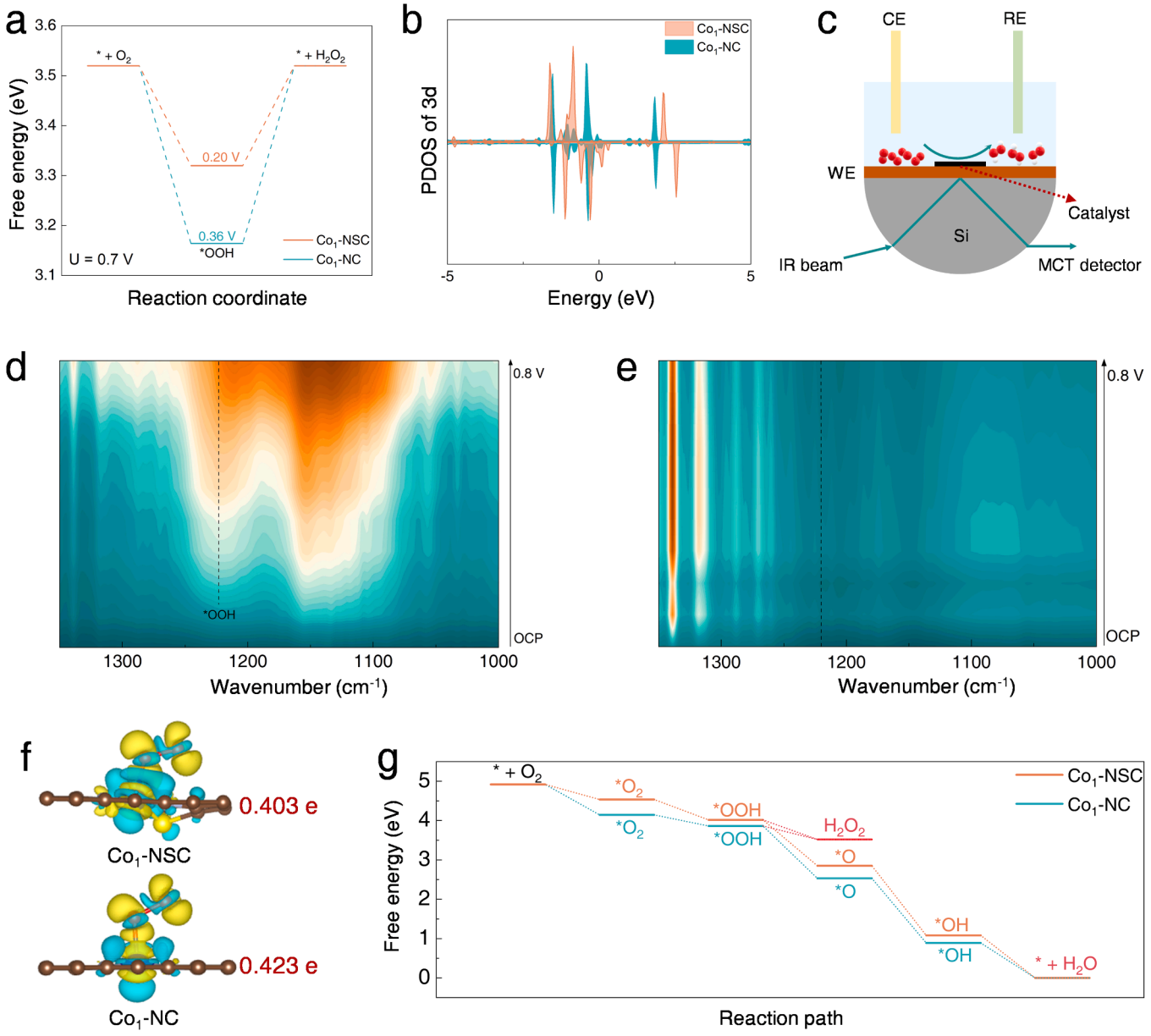

Fig. 4. Theoretical analysis. (a) Gibbs free energy diagram for 2e^- ORR at 0.7 V *vs.* RHE on Co_1-NSC. (b) PDOS and corresponding calculated dband centers of Co 3d for Co_1-NSC and Co_1-NC models. (c) An illustration of *in-situ* ATR-SEIRAS measurements. *In-situ* ATR-SEIRAS spectrum of (d) Co_1-NSC and (e) Co_1-NC. (f) The difference of electron density for *OOH intermediates adsorbed on Co_1-NSC and Co_1-NC models, the cyan and yellow areas represent electron loss and accumulation, respectively. (g) Free energy diagram for ORR, including the 4e^- and 2e^- ORR pathways on Co_1-NSC and Co_1-NC models.

generation *via* the 2e^- ORR pathway. Additionally, in the volcano plot plotted as a function of ΔG*OOH (Fig. S28), Co_1-NC is located on the left side of the volcano peak, indicating that Co_1-NC has strong *OOH adsorption, leading to low 2e^- ORR selectivity. Co_1-NSC, on the other hand, approaches the volcano peak, indicating that its *OOH adsorption strength is appropriate. Analysis of the Co spin density for both Co_1-N_4 and Co_1-N_3S_1 configurations indicates that synergistic coordination doping of S in Co-N_4 significantly enhances the spin density of Co atoms (Fig. S29). Furthermore, partial density of states (PDOS) analysis shows that a noticeable spin polarization phenomenon occurs when cobalt atoms transition from Co_1N_4 coordination to $Co_1N_3S_1$ coordination (Fig. 4b). It is worth noting that the D-band center of cobalt atoms in Co_1-NSC (-1.054 eV) is lower than that in Co_1-NC (-0.954 eV) (Table S5). The shift of the D-band center caused by the elevated spin state is an inevitable result of electronic rearrangement and orbital energy level adjustments induced by the weakened coordination field. The weak-field ligands and changes in coordination symmetry reduce the crystal field splitting, which not only alters the electronic filling of the Co site but also lowers the average energy of its D-orbitals, causing the overall energy level of the Co 3d orbitals to shift toward lower energy levels [63–65]. The decrease in the D-band center weakens the adsorption strength of the cobalt site on *OOH, which is conducive to desorption and the formation of H_2O_2. *In situ* attenuated total reflectance surface-enhanced infrared absorption spectroscopy (ATR-SEIRAS) analysis further validates this computational result (Fig. 4c). During the negative potential change, Co_1-NSC exhibits a characteristic absorption band at approximately 1220 cm^{-1} (Fig. 4d), which is attributed to the O-O stretching vibration of the *OOH intermediate adsorbed on the cobalt site surface (OOHad) [66], and the peak intensity increases with the rise in reduction potential. Conversely, this absorption band is nearly absent on the Co_1-NC surface (Fig. 4e) This may be attributed to the Co sites promoting O-O bond cleavage, making it difficult to form *OOH intermediate species, thereby leading to the 4e^- reaction pathway for H_2O formation. Bader charge analysis of *OOH adsorption at the Co site reveals two distinct behavioral patterns of active sites and reaction intermediates in the two configurations. As shown in Fig. 4f, Co_1-NSC exhibits more electron-deficient regions (dark blue areas), while Co_1-NC displays more electron-rich regions (yellow areas) at the cobalt site. Furthermore, the Bader charge value for Co_1-NSC (0.403 e) is lower than that for Co_1-NC (0.423 e) (Table S6), indicating stronger interaction

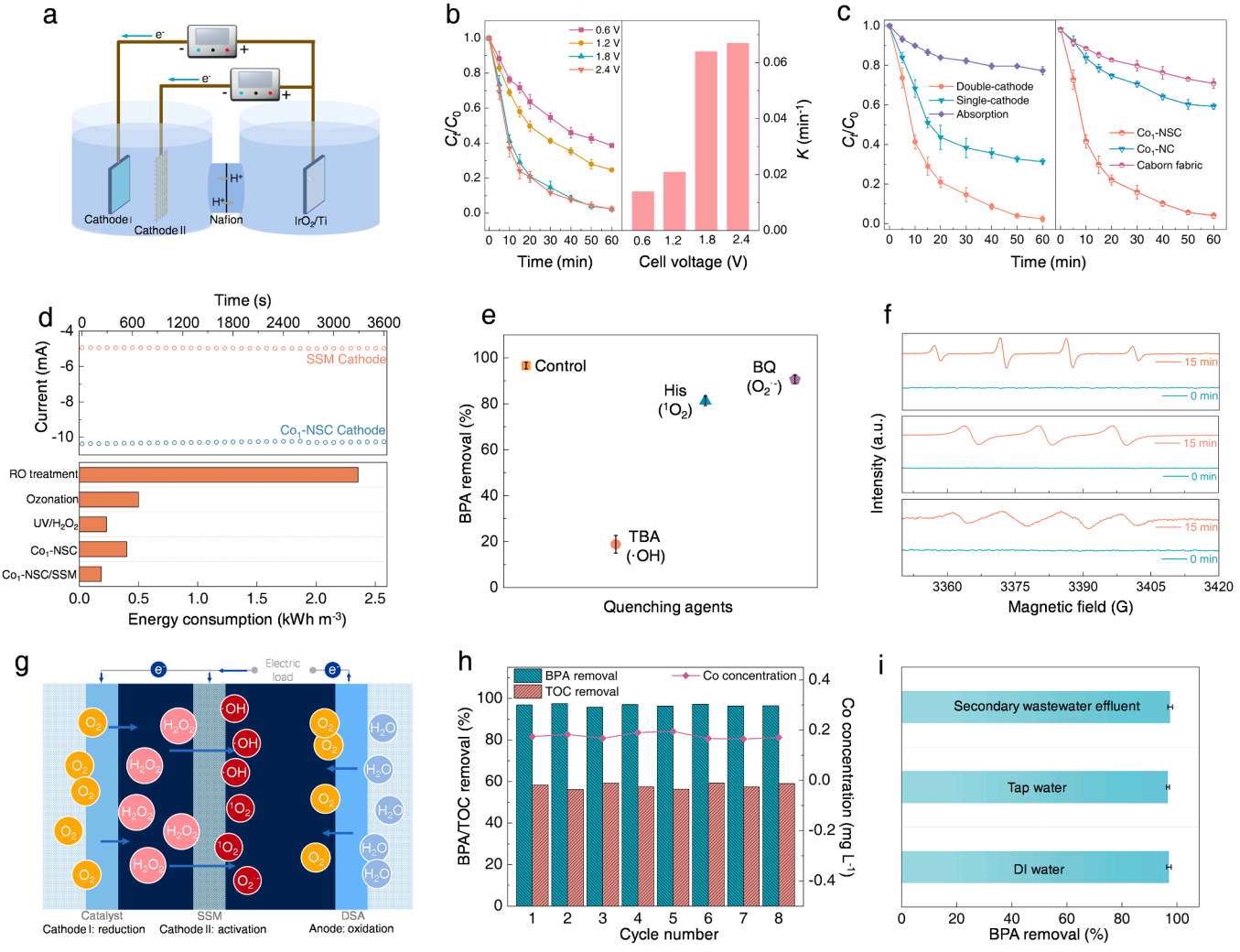

Fig. 5. High-spin Co sites enhance the degradation capacity in the sequential dual-cathode electro-Fenton system. (a) Schematic diagram of a sequential dual-cathode organic pollutant degradation system (b) BPA degradation efficiency (C_t/C_0) and corresponding degradation rate constants under different applied voltages. (c) BPA degradation efficiency in different systems. (d) Chronoamperometry of two cathodes when cell voltage is 1.8 V and calculated degradation energy consumption with other degradation systems. (e) Effect of adding TBA (100 mM), His (20 mM) and BQ (20 mM) on BPA degradation. (f) The EPR spectra of DMPO-·OH, TEMP-$^1O_2$ and DMPO-$O_2^{\cdot-}$. (g) Schematic diagram of the catalytic degradation process of the dual-cathode EF system. (h) Removal of BPA and TOC and leaching concentration of Co in the system during eight cycles. (i) BPA degradation in different water matrices. Conditions: [BPA] = 10 mg L^{-1}, [H_2SO_4] = 0.05 M, [O_2 input rate] = 30 mL min^{-1}, [Cell voltage] = 1.8 V.

between oxygen-containing intermediates and Co sites on Co_1-NC. This promotes O-O bond cleavage, favoring the 4e^- pathway. In contrast, the weaker electron interactions on Co_1-NSC ensure smooth desorption of *OOH and subsequent H_2O_2 formation, thereby promoting the 2e^- ORR pathway [67]. Free energy diagrams for the ORR (Fig. 4g) further demonstrate that Co_1-NSC preferentially follows the 2e^- ORR pathway to generate H_2O_2, whereas Co_1-NC exhibits a thermodynamic preference for forming H_2O *via* the 4e^- ORR pathway.

Given that the prepared Co_1-NSC exhibits excellent 2e^- ORR activity, selectivity, and bulk electrolytic synthesis of H_2O_2, we installed it in a dual-cathode heterogeneous electro-Fenton (EF) system for pollutant degradation. Co_1-NSC was loaded onto CFF (Co_1-NSC/CFF) as the ORR cathode. The H_2O_2-activated cathode is stainless steel mesh (SSM) (Fig. 5a). Bisphenol A (BPA), one of the typical endocrine disruptors, was selected as the target pollutant. First, we investigated the effect of applied cell voltage on the degradation rate of BPA. As shown in Fig. 5b and Fig. S30, the degradation rate of BPA increases with rising cell voltage (0.6 V–1.8 V) which due to the increased applied potential leads to greater H_2O_2 generation at the ORR cathode, directly elevating reactive oxygen species (ROS) concentration. However, when the cell voltage was further increased to 2.4 V, the degradation rate of BPA showed no significant improvement. This may be due to the excessive H_2O_2 in the solution consuming ROS (such as ·OH), thereby limiting the further increase in the degradation rate of the treatment system (Fig. S31) [68]. Next, at a voltage of 1.8 V, after 60 min of treatment, only approximately 22% of BPA was adsorbed and removed. Approximately 98% of BPA was degraded in the dual-electrode electro-Fenton system, with a degradation efficiency of approximately 70% in the single-cathode system (Fig. 5c). The pseudo-first-order kinetics demonstrate that the dual-cathode system (0.064 min^{-1}) degrades BPA at rates 20 and 3.6 times faster than the adsorption (0.003 min^{-1}) and single-cathode systems (0.018 min^{-1}), respectively. (Fig. S32). To determine the current distribution during the operation of the dual-cathode EF system, we simultaneously recorded the current of Co_1-NSC/CFF (first cathode) and SSM (second cathode) (Fig. 5d). The Co_1-NSC/CFF cathode consumed the majority of the current (~10 mA), which generated H_2O_2 through the 2e^- ORR, while the SSM cathode consumed a smaller current (~5 mA). This smaller current is associated with the activation of H_2O_2 by the SSM cathode to produce ROS, thereby inhibiting competitive reactions such as oxygen reduction. In addition, based on the current distribution across the two cathodes and the amount of BPA degradation, we calculated the degradation energy consumption of the dual-cathode EF system. The dual-cathode electro-Fenton system using the Co_1-NSC/CFF electrode had an energy consumption of 0.185 kWh m^{-3}, outperforming the system using the Co_1-NC/CFF electrode (0.400 kWh m^{-3}). Notably, the energy consumption of the dual-cathode EF system is comparable to or lower than values reported for conventional treatment technologies such as UV/H_2O_2 (0.230 kWh m^{-3}), ozonation (0.500 kWh m^{-3}), and reverse osmosis (RO) treatment (2.355 kWh m^{-3}) [69,70], highlighting its ability to achieve efficient pollutant degradation with relatively low energy input. Subsequently, tert-butanol (TBA), L-histidine (His) and p-benzoquinone (BQ) were used as quenchers for ·OH, $^1O_2$, and $O_2^{\cdot-}$, respectively, in quenching experiments [71]. As depicted in Fig. 5e, the degradation efficiency of BPA was significantly suppressed upon addition of TBA, indicating that ·OH plays a dominant role in organic compound degradation. EPR spectroscopy further confirmed the presence of ·OH, $^1O_2$, and $O_2^{\cdot-}$ (Fig. 5f). As expected, no signals were observed when no potential was applied (0 min). After 15 min of reaction, a characteristic high-intensity quadruplet signals corresponding to the hydroxyl adduct of 5,5-dimethyl-1-pyrroline-N-oxide (DMPO) was observed, indicating the formation of ·OH in the system. EPR analysis using 2,2,6,6-tetramethylpiperidine (TEMP) as a spin trap revealed a triplet signal attributed to the TEMP-$^1O_2$ adduct, signifying $^1O_2$ formation. Additionally, DMPO-$O_2^{\cdot-}$ adducts were identified using DMPO as the trapping agent, indicating superoxide radical ($O_2^{\cdot-}$) generation. As described above, O_2 is *in-situ* converted into H_2O_2 *via* the 2e^- ORR on Co_1-NSC. It is therefore proposed that the *in situ*-generated H_2O_2 is further activated *via* electron transfer on the SSM cathode to produce ROS, which subsequently attack organic pollutants and lead to their removal (Fig. 5g). Ultraperformance liquid chromatography-high-resolution mass spectrometry was employed to identify degradation intermediates of BPA (Fig. S33, Table S7). Based on the types of intermediates, a plausible evolutionary mechanism for BPA is demonstrated (Fig. S34). In the first step, the hydroxyl radical generated upon activation of H_2O_2 attacks the benzene ring of the BPA molecule, forming unstable hydroxylated BPA derivatives. Subsequently, this unstable product undergoes a bridge-breaking reaction, yielding monobenzene ring products of 4-isopropylphenol and phenol. These compounds undergo ring-opening reactions to form a series of downstream short-chain acids including maleic acid, divinyloxyethena and oxalic acid. Ultimately, these short-chain acids decompose into CO_2 and H_2O. Additionally, the system demonstrated excellent degradation stability, with BPA degradation efficiency maintained at 96.3% after eight electrochemical treatments (Fig. 5h). Furthermore, TOC removal stabilized at ~60%, indicating that the degradation system possesses excellent mineralization capacity for organic pollutants. In addition, we used ICP-MS to quantitatively determine the Co concentration in the solution after degradation. Throughout the eight degradation cycles, the Co concentration remained below 0.2 mg L^{-1}. This value is significantly lower than the maximum allowable concentration of total cobalt (1.0 mg L^{-1}) in wastewater discharges specified by the Chinese national standard GB 25467–2010, which is attributed to the high stability exhibited by Co_1-NSC during long-time electrolysis experiments. The dual-cathode treatment system also maintained stable BPA removal efficiency in tap water and secondary effluent from municipal wastewater treatment plants (Fig. 5i), demonstrating its practical application potential in complex water conditions.

3. Conclusion

In summary, this work employs a coordination doping strategy to regulate the spin-state of active sites, thereby optimizing the adsorption strength of *OOH and promoting H_2O_2 generation. We construct a catalyst with dispersed cobalt atoms anchored on a nitrogen/sulfur co-doped carbon substrate (Co_1-NSC), which exhibits excellent 2e^- ORR selectivity (92.3%) and bulk synthesis of H_2O_2 (5.56 mol g_{cat}^{-1} h^{-1} and the corresponding FE of ~90% in the flow cell). Furthermore, the sequential dual-cathode EF system constructed using Co_1-NSC as the ORR catalyst demonstrated outstanding BPA removal efficiency (~98%), with a degradation rate constant (0.064 min^{-1}), which is 3.6 times higher than that of Co_1-NC, and its energy consumption (0.185 kWh m^{-3}) was also lower than conventional treatment methods. Experimental results and theoretical calculations indicate that the incorporation of S alters the spin-orbit splitting (ΔE) of Co sites, inducing a transition of the Co site's spin state from low spin to high spin, lowering the d-band center of Co atoms, weakening the adsorption strength of *OOH at active sites, and promoting the desorption of *OOH to form H_2O_2 rather than further reduction to H_2O. This work provides a strategy for designing and developing catalysts with excellent 2e^- ORR performance through spin engineering.

4. Experimental section

Chemicals. Urea (CH_4N_2O, 99%), i-carrageenan, cobalt nitrate ($Co(NO_3)_2{\cdot}6\,H_2O$, 99.99%), aniline (C_6H_7N, 99.9%), ammonium persulphate ($(NH_4)_2S_2O_8$, ≥ 96%) cobalt chloride ($CoCl_2{\cdot}6\,H_2O$, 99.99%) were obtained from Aladdin Chemistry Co. Ltd. (Shanghai, China). Ketjen Black ECP-600 JD was purchased from Hangzhou Chuangshi Biotechnology Co., Ltd. (Hangzhou, China). Sulphuric acid (H_2SO_4, 99.7%) and hydrochloric acid (HCl, 99.7%) were purchased from Tianjin Bohua Chemical Reagent Co. Ltd. (Tianjin, China). Cerium

sulphate ($Ce(SO_4)_2$ 4 H_2O, 99.99%) was purchased from Shanghai BiDe Pharmaceutical Technology Co. Ltd. (Shanghai, China). Hydrophobic carbon fiber fabric (CFF) was purchased from Yanshen Technology Co., Ltd. (Tianjin, China). All chemicals were purchased from commercial sources and used directly without further purification.

Preparation of Co_1-NSC. 2 g of urea was added to 100 mL of deionized water at 80 °C, and then 4 g of i-carrageenan was slowly dripped into the above urea solution and stirred at 80 °C for 1 h. Then 0.2 g of Co $(NO_3)_2$·9 H_2O was added to the above solution and stirred at 80 °C for 5 h. The obtained hydrogel of carrageenan-urea-Co was frozen and dehydrated by freeze-drying process to obtain the carrageenan-urea-Co aerogel. The aerogel was pyrolysed in N_2 atmosphere at 900 °C for 2 h at a heating rate of 5 °C/min^{-1}, and then the resulting sample was soaked in 1.0 M HCl solution for 10 h to remove K_2S and CaS particles to obtain Co_1-NSC.

Preparation of Co_1-NC. Dissolve 2 mL of aniline in 200 mL of 0.5 M HCl solution. Then, add 30 mL of 0.6 M $CoCl_2$ solution dropwise. After stirring at 4°C for 60 min, slowly add 20 mL of 1.1 M $(NH_4)_2S_2O_8$ solution to polymerize the aniline. Next, add 400 mg of Ketjen Black ECP-600 JD to the above solution. After stirring at room temperature for 2 days, further collect the desired precursor and dry it under vacuum at 60°C. Then, decompose the precursor at 900°C for 1 h in an Ar atmosphere. Finally, the resulting product was soaked in 2.0 H_2SO_4 at 60°C for 12 h, thoroughly washed with deionized water, and vacuum-dried at 60°C.

Preparation of NSC. The control sample of NSC was prepared similarly to Co_1-NSC but without the addition of $Co(NO_3)_2$·6 H_2O.

Effective magnetic moment (μ_{eff}) calculation is as follows in Eqs. 4 and 5:

$$\chi = \frac{C}{T-\Theta} + \quad \chi 0 \tag{4}$$

where χ is susceptibility, χ_0 is a constant whose origin is a temperature independent contribution to susceptibility, Θ is Curie Weiss temperature. T is experimental temperature.

$$\mu_{eff} = \sqrt{8C}\mu_B = g_{\mu B}\sqrt{S_{LS}(S_{LS}+1)V_{LS} + S_{HS}(S_{HS}+1)V_{HS}} \tag{5}$$

where μ_B is Bohr magneton, g is the Landé g-factor (g = 2 for electron), C is Curie constant, S_{LS} and S_{HS} are total spin angular momentum of L_S and H_S, respectively. The V_{LS} and V_{HS} are the fractions of L_S and H_S, respectively.

Electrochemical measurements. The ORR catalytic performances were measured on a CHI 760E electrochemical workstation (CH Instrumental Corporation, Shanghai, China) with a rotating ring-disk electrode setup (RRDE, Pine Instruments Corporation). The effective area of the platinum disc is 0.247 cm^2, and the effective area of the platinum ring is 0.185 cm^2.The catalyst ink was prepared by dispersing 2.5 mg as-synthesized catalyst into 980 μL of ethanol and 20 μL of Nafion solution (5.0 wt%), followed by ultrasonication for 30 min. Then 10 μL of catalyst ink was drop-casted onto the disk electrode and naturally dried. An Ag/AgCl electrode and graphite rod were used as the reference and counter electrode, respectively. 0.05 H_2SO_4 was used as the electrolyte. The linear sweep voltammetry (LSV) curves were recorded in O_2-saturated condition with a scan rate of 10 mV s^{-1} at 1600 rpm and the potential of the Pt ring electrode was set at 1.2 V *vs.* RHE to detect as-generated H_2O_2 on disk electrode. The H_2O_2 selectivity and electron transfer number (*n*) on the RRDE were calculated using the following Eqs. 6 and 7:

$$\text{Selectivity (\%)} = 200\times (I_r/N_c)/(I_d+I_r/N_c) \tag{6}$$

$$n = 4\times I_d/(I_d+I_r/N_c) \tag{7}$$

where I_r and I_d are the ring current and the disk current, respectively; and N_c is the collection efficiency of the ring electrode (0.37).

The kinetic current density (j_k) was calculated according to the Koutecký-Levich equation:

$$1/j = 1/j_l + 1/j_k \tag{8}$$

where j denotes the measured current and jl denotes the limiting current. j_l can be obtained from the Levich equation containing the total number of electrons transferred (n) set by RRDE:

$$j_l = 0.62\times n \times F\times A\times D_o^{2/3}\times\omega^{1/2}\times \upsilon^{-1/6}\times C_o \tag{9}$$

where F denotes Faraday constant (96,485 mol^{-1}); A denotes the geometric area of the disk electrode (0.247 cm^2); D_o denotes the diffusion coefficient of O_2 in the electrolyte at 298 K (1.85×10^{-5} cm^2 s^{-1}); ω denotes the electrode speed (rad s^{-1}); υ denotes the kinematic viscosity of O_2 (0.89×10^{-2} cm^2 s^{-1}) and C_o for O_2 concentration (1.21×10^{-6} mol cm^{-3}).

For the metal site masking experiment, LSV curve data for Co_1-NSC were first collected in an O_2-saturated 0.05 M H_2SO_4 electrolyte. After the test, 10 mM KSCN was added to the electrolyte, and the LSV test was performed again. Subsequently, the catalyst-loaded electrode was thoroughly rinsed with deionized water and transferred to fresh 0.05 M H_2SO_4 electrolyte free of SCN^-, and ORR activity was retested to observe the recovery.

The bulk synthesis of H_2O_2 was conducted in a two-compartment three-electrode H-cell separated by a Nafion 117 membrane. Each compartment was filled with 10 mL of 0.05 M H_2SO_4 and the cathode was purged with O_2 for at least 30 min to reach saturation. The working electrode was fabricated by drop-casting the Co_1-NSC ink onto 1.0×1.0 cm^2 CFF with a catalyst loading amount of 0.15 mg cm^{-2}. Ag/AgCl and Pt sheet were utilized as reference and counter electrodes, respectively. Then, bulk ORR electrolysis was conducted at various applied potentials for 1 h. Subsequently, the H_2O_2 yield operated at different potentials was quantified according to the ceric sulfate titration method as Eq. 10:

$$2Ce^{4+} + H_2O_2 \rightarrow 2Ce^{3+} + 2H^+ + O_2 \tag{10}$$

The yield of H_2O_2 can be calculated by the following Eq. 11:

$$C_{H2O2} = [V_{Ce4+}\times[Ce^{4+}]_{before} - (V_{Ce4+} + V_{electrolyte}) \times [Ce^{4+}]_{after}]/(2\times V_{electrolyte}) \tag{11}$$

where V_{Ce4+} is the volume of added $Ce(SO_4)_2$ solution; $[Ce^{4+}]_{before}$ and $[Ce^{4+}]_{after}$ are the concentration of Ce^{4+} before and after reaction, respectively; $V_{electrolyte}$ is the volume of injected electrolyte after reaction. The standard concentration-absorbance curve was obtained by linearly fitting the absorbance values at 319 nm for various known concentrations of Ce^{4+}. The Faradaic efficiency (FE) value is calculated according to Eq. 12:

$$\text{FE (\%)} = (2\times C\times V\times F)/Q \times 100\% \tag{12}$$

where F is the Faraday constant (96485 C mol^{-1}); C is the concentration of generated H_2O_2 (mol L^{-1}); V is the volume of electrolyte (L); Q is the passed charge during the electrolysis (C).

The catalyst stability performance test was conducted in an H-type cell. The CFF loaded with Co_1-NSC was removed after operating for a specific time (2 h), washed with deionized (DI) water, dried in an oven, and then the experiment was repeated.

A standard three-electrode three-phase flow cell system was assembled on a CHI660E electrochemical workstation using a gas diffusion electrode (GDE) as the working electrode, a platinum electrode as the reference electrode, and an Ag/AgCl electrode as the counter electrode. The catalyst ink was prepared by dispersing 10 mg of the sample in 1 mL of anhydrous ethanol containing 40 μL of Nafion solution to form a uniform suspension. Next, a drop of the uniform catalyst ink was applied to a GDE with an area of 2×2 cm^2 (effective area of 1×1 cm^2). The catalyst loading was determined to be 0.3 mg cm^{-2}. Both the electrolyte and the anolyte were 0.05 M H_2SO_4 solutions. The electrolyte was freshly prepared before each measurement. The cell was separated by an

anion-exchange membrane. Throughout the measurement, the oxygen gas flow rate was maintained at 20 mL min^{-1}. The H_2O_2 generation rate was determined using the ceric sulfate titration method. None of the electrochemical tests were performed with infrared compensation.

Experimental characterizations. The crystal structure of the catalyst was characterized by X-ray powdered diffraction (XRD) *via* a Rigaku D/Max 2200PC with Cu Kα radiation. The morphology and microstructure of the catalyst were recorded by high-resolution transmission electron microscopy (TEM) through a JEOL JEM-ARM200F NEOARM at an accelerating voltage of 200 kV. HAADF-STEM characterization was performed on the STEM mode of an FEI Titan Themis G1, equipped with a dual aberration corrector and four EDS detectors, each of which has an effective area of 30 mm^2 for detecting the EDS signals. X-ray photoelectron spectroscopy (XPS) was measured by a Thermal ESCALAB Xi+ electron spectrometer using Al Kα X-ray source under an ultrahigh vacuum. N_2 adsorption-desorption isotherms are recorded with Autosorb-IQ Automated Gas Sorption Analyzer (Quantachrome). Cobalt content in the catalyst and solution was measured using inductively coupled plasma atomic emission spectroscopy (ICP-AES; 725-ES, Varian). Electrochemical characterization, including electrochemical impedance spectroscopy (EIS), cyclic voltammetry (CV), and amperometric i-t curves, was performed using a CHI660E electrochemical workstation. Intermediate products of BPA degradation were determined using ultra-high-performance liquid chromatography-high-resolution mass spectrometry (UPLC-HRMS, Orbitrap Fusion, Thermo Fisher Scientific, USA). Ten microliters of the extract were automatically injected into the UPLC-HRMS system using a Waters C18 column (150 mm × 10 mm, 5 μm). The mobile phase consisted of acetonitrile and water (both containing 0.1% formic acid), with a flow rate of 0.4 mL min^{-1}.

Electrochemical in situ Raman spectroscopy analysis. In situ Raman spectroscopy of the catalyst was performed using an HR Evolution spectrophotometer (HORIBA Scientific Inc.). The laser excitation wavelength was 532 nm. The catalyst, anhydrous ethanol, and Nafion solution were mixed to form a catalyst ink. The ultrasonicated ink was coated onto the CP (1.5 cm × 1.5 cm, catalyst loading of 1 cm^{-2}) and dried. During the test, a 0.05 M H_2SO_4 solution saturated with O_2 was used as the electrolyte. The sample spectra were collected in increments of 0.2 V within the range of 0.8–0 V relative to the reference electrode.

Electrochemical in situ attenuated total reflectance surface-enhanced infrared absorption spectroscopy (ATR-SEIRAS). In situ ATR-SEIRAS measurements were conducted using a Thermo Scientific Thermo 8700 spectrometer (Thermo Scientific, USA) equipped with a liquid nitrogen-cooled MCT-A detector. In an acidic solution (0.05 M H_2SO_4), the synthesized electrocatalyst, Ag/AgCl electrode, and platinum wire were employed as the working electrode, reference electrode, and counter electrode, respectively. A standard three-electrode system was utilized to perform *in-situ* ATR-SEIRAS electrochemical spectroscopy. FTIR measurements were carried out in the potential range from 0 to 0.8 V in 0.1 V increment.

X-ray absorption spectroscopy (XAS) data collection and analysis. The X-ray absorption fine structure (XAFS) spectra were collected at 1W1B station in Beijing Synchrotron Radiation Facility (BSRF). The storage rings of BSRF were operated at 2.5 GeV with an average current of 250 mA. Using Si (111) double-crystal monochromator, the data collection was carried out in transmission/fluorescence mode using ionization chamber. All spectra were collected in ambient conditions. The acquired EXAFS data were processed according to the standard procedures using the ATHENA module implemented in the IFEFFIT software packages. The k^3-weighted EXAFS spectra were obtained by subtracting the post-edge background from the overall absorption and then normalizing with respect to the edge-jump step. Subsequently, k^3-weighted χ(k) data were Fourier transformed to real (R) space using a Hanning windows (dk = 1.0 $Å^{-1}$) to separate the EXAFS contributions from different coordination shells. To obtain the quantitative structural parameters around central atoms, least-squares curve parameter fitting was performed using the ARTEMIS module of the IFEFFIT software packages.

Sequential Dual-Cathode Degradation Experiment. The sequential dual-cathode EF experiment was conducted in a H-type electrolysis device with two chambers, each with a volume of 40 mL. Specifically, an IrO_2/Ti plate (9 cm^{-2}) was used as the anode, and Co_1-NSC/CFF (Cathode I) was employed to generate hydrogen peroxide. Oxygen was pumped into the solution near Cathode I at a rate of 30 mL per minute to continuously produce hydrogen peroxide. A stainless-steel mesh cathode (Cathode II) was used to activate H_2O_2. The distance between the two cathodes is 2 cm. The electrochemical workstation provides a DC power supply and controls the cell voltage (0–2.4 V); the voltages of both cathodes are maintained at the same value.

The energy consumption was calculated as the electrical energy per order (EEO (kWh m^{-3})) according to the following Eq. 13:

$$E_{EO} = \frac{t(I_1 + I_2)E_{cell}}{1000 \quad V\log\frac{C_0}{C_t}} \tag{13}$$

where E_{cell} is the applied voltage (V), I_1 and I_2 are the currents (A) of cathode I and cathode II, respectively, t is the treatment duration (h), V is the volume of water (m^3), and C_0 and C_t are the initial and final BPA concentrations (mg L^{-1}), respectively.

Ultraperformance liquid chromatography–high-resolution mass spectrometry. The degradation intermediates of BPA were identified by ultraperformance liquid chromatography–high-resolution mass spectrometry (UPLC–HRMS, Orbitrap Fusion, Thermo, USA). The eluent was composed of 0.1% methanoic acid and acetonitrile, and the flow rate was 0.2 mL min^{-1}.

DFT Calculate. All first-principles calculations in this paper were performed using the Vienna ab-initio simulation package (VASP) [72]. The Projector Augmented Wave (PAW) method [73] was used as the basis functions to describe the interactions between electrons and ions. Under the Generalized Gradient Approximation (GGA), the Perdew-Burke-Ernzerhof (PBE) functional [74] was employed to handle the exchange-correlation effects of electrons, and the DFT-D3 was used to correct the van der Waals interactions. The k-points were set to be 2 × 2 × 1 with Gamma centered grids for all structures for geometry optimization. The interruption criterion for the electronic self-consistent cycle is set to 10–5 eV, the maximum force on each atom was limited to 0.02 eV/Å, and the cutoff energy for the plane wave basis set was set to 400 eV. The $2e^-$ ORR mechanism for producing H_2O_2 comprises of two elementary steps are shown in Eqs. 14 and 15 [75]:

$$* + O_{2(g)} + \quad H^+ + e^- \quad \longrightarrow OOH* \tag{14}$$

$$OOH* + \quad H^+ + \quad e^- \quad \longrightarrow \quad H_2O_{2(l)} + \quad * \tag{15}$$

The asterisk (*) denotes the active site of the catalyst.

The free energy of adsorbed specie, computed based on computational hydrogen electrode (CHE) model, is defined as (Eq. 16):

$$G = E + ZPE - TS \tag{16}$$

where E is the DFT-derived total ground state energy of a system. ZPE is the zero-point energy correction and TS is the entropy correction computed with standard methods and used to convert E into free energy (G) at 298.15 K.

CRediT authorship contribution statement

Ligang Wang: Writing – review & editing, Writing – original draft, Visualization, Validation, Software, Resources, Methodology, Investigation, Funding acquisition, Formal analysis, Data curation, Conceptualization. **Xiaoyu Zhang:** Visualization, Data curation. **Zhong Jin:** Writing – review & editing, Supervision, Resources, Funding acquisition, Conceptualization. **Kewang Liu:** Writing – original draft, Visualization, Methodology, Investigation, Formal analysis, Data curation,

Conceptualization. **Sihui Zhan:** Writing – review & editing, Supervision, Software, Resources, Project administration, Methodology, Funding acquisition, Conceptualization. **Pengfei Wang:** Writing – review & editing, Validation, Supervision, Software, Resources, Project administration, Methodology, Investigation, Funding acquisition, Formal analysis. **Weizhao Yan:** Writing – review & editing. **Limin Shen:** Writing – review & editing. **Haiyin Zhan:** Data curation. **Huaizhu Wang:** Writing – review & editing.

Declaration of Competing Interest

The authors declare that they have no known competing financial interests or personal relationships that could have appeared to influence the work reported in this paper.

Acknowledgments

This work was supported by the Natural Science Foundation of China projects (Grant Nos. 22225604, U24A20518, 22422605, U25A20628, 22561160129, 22479074, 22475096), the Tianjin Commission of Science and Technology as key critical technologies R&D projects (Grant No. 23YFZCSN00010 and 24YFZCSN00050), the Frontiers Science Center for New Organic Matter (Grant No. 63181206), Young Scientific and Technological Talents (Level Two) in Tianjin (QN20230206), the Fundamental Research Funds for the Central Universities, Nankai University (63253207) and Haihe Laboratory of Sustainable Chemical Transformations, the Equipment Pre-Research and Ministry of Education Joint Fund (8091B02052407), the Fundamental Research Program Key Project of Jiangsu Province (BK20253008), the Science and Technology Major Project of Jiangsu Province (BG2024013), the Scientific and Technological Achievements Transformation Special Fund of Jiangsu Province (BA2023037), the Academic Degree and Postgraduate Education Reforming Project of Jiangsu Province (JGKT24_C001), the Key Core Technology Open Competition Project of Suzhou City (SYG2024122), the Open Research Fund of Suzhou Laboratory (SZLAB-1308–2024-TS005), the Chenzhou National Sustainable Development Agenda Innovation Demonstration Zone Provincial Special Project (2023sfq11, 2025sfq38), and the Fundamental Research Funds for the Central Universities and Nanjing University International Collaboration Initiative (020514380354).

Appendix A. Supporting information

Supplementary data associated with this article can be found in the online version at doi:10.1016/j.nanoen.2026.112038.

Data availability

Data will be made available on request.

References

[1] R.P. Schwarzenbach, B.I. Escher, K. Fenner, T.B. Hofstetter, C.A. Johnson, U. V. Gunten, B. Wehrli, The challenge of micropollutants in aquatic systems, Science 313 (5790) (2006) 1072–1077.
[2] W. Zhang, X. Hao, X. Liu, M. Chu, S. Li, X. Wang, F. Jiang, L. Wang, Q. Zhang, J. Chen, D. Wang, M. Cao, Photocatalytic conversion of polyester-derived alcohol into value-added chemicals by engineering atomically dispersed Pd catalyst, Angew. Chem. Int. Ed. 64 (18) (2025) e202500814.
[3] Y. Liu, P. Yan, X. Li, Q. Li, S. Li, H. Han, M. Chu, J. Fu, M. Cao, P. Xu, Q. Zhang, L. He, J. Chen, Selective recycling of mixed polyesters *via* heterogeneous photothermal catalysis, Adv. Mater. 34 (7) (2025) 2412740.
[4] F. Wang, L. Xiang, K.S. Leung, M. Elsner, Y. Zhang, Y. Guo, B. Pan, H. Sun, T. An, G. Ying, B.W. Brooks, D. Hou, D.E. Helbling, J. Sun, H. Qiu, T.M. Vogel, W. Zhang, Y. Gao, M.J. Simpson, Y. Luo, S.X. Chang, G. Su, B.M. Wong, T. Fu, D. Zhu, K. J. Jobst, C. Ge, F. Coulon, J.D. Harindintwali, X. Zeng, H. Wang, Y. Fu, Z. Wei, R. Lohmann, C. Chen, Y. Song, C. Sanchez-Cid, Y. Wang, A.E. Naggar, Y. Yao, Y. Huang, J.C.F. Law, C. Gu, H. Shen, Y. Gao, C. Qin, H. Li, T. Zhang, N. Corcoll, M. Liu, D.S. Alessi, H. Li, K.K. Brandt, Y. Pico, C. Gu, J. Guo, J. Su, P. Corvini, M. Ye, T.R. Santos, H. He, Y. Yang, M. Tong, W. Zhang, F. Suanon, F. Brahushi, Z. Wang, S.A. Hashsham, M. Virta, Q. Yuan, G. Jiang, L.A. Tremblay, Q. Bu, J. Wu, W. Peijnenburg, E. Topp, X. Cao, X. Jiang, M. Zheng, T. Zhang, Y. Luo, L. Zhu, X. Li, D. Barceló, J. Chen, B. Xing, W. Amelung, Z. Cai, R. Naidu, Q. Shen, J. Pawliszyn, Y. Zhu, A. Schaeffer, M.C. Rillig, F. Wu, G. Yu, J.M. Tiedje, Emerging contaminants: a one health perspective, Innovation 5 (4) (2024) 100612.
[5] D. Wen, R. Fu, Q. Li, Removal of inorganic contaminants in soil by electrokinetic remediation technologies: A review, J. Hazard. Mater. 401 (5) (2020) 123345.
[6] J. Pesqueira, M. Pereira, A. Silva, Environmental impact assessment of advanced urban wastewater treatment technologies for the removal of priority substances and contaminants of emerging concern: A review, J. Clean. Prod. 261 (10) (2020) 121078.
[7] T. Alvarino, S. Suarez, J. Lema, F. Omil, Understanding the sorption and biotransformation of organic micropollutants in innovative biological wastewater treatment technologies, Sci. Total Environ. 615 (15) (2017) 297–306.
[8] C. Sheng, A. Nnanna, Y. Liu, J. Vargo, Removal of trace pharmaceuticals from water using coagulation and powdered activated carbon as pretreatment to ultrafiltration membrane system, Sci. Total Environ. 550 (15) (2016) 1075–1083.
[9] Ike, I., Karanfil, T., Cho, J., Hur, J. Oxidation byproducts from the degradation of dissolved organic matter by advanced oxidation processes–A critical review. Water Res. 201, 164 (1), 114929.
[10] P. Rout, T. Zhang, P. Bhunia, R. Surampalli, Treatment technologies for emerging contaminants in wastewater treatment plants: A review, Sci. Total Environ. 753 (20) (2021) 141990.
[11] L. Rizzo, S. Malato, D. Antakyali, V.G. Beretsou, M.B. Đolić, W. Gernjak, E. Heath, I.I. Tumbas, P. Karaolia, A.R.L. Ribeiro, G. Mascolo, C.S. McArdell, H. Schaar, A.M. T. Silva, D.F. Kassinos, Consolidated vs new advanced treatment methods for the removal of contaminants of emerging concern from urban wastewater, Sci. Total Environ. 655 (10) (2018) 986–1008.
[12] B. Hodges, E. Cates, J. Kim, Challenges and prospects of advanced oxidation water treatment processes using catalytic nanomaterials, Nat. Nanotechnol. 13 (2018) 642–650.
[13] J. Xu, X. Zheng, Z. Feng, Z. Lu, Z. Zhang, W. Huang, Y. Li, D. Vuckovic, Y. Li, S. Dai, G. Chen, K. Wang, H. Wang, J.K. Chen, W. Mitch, Y. Cui, Organic wastewater treatment by a single-atom catalyst and electrolytically produced H_2O_2, Nat. Sustain. 4 (2020) 233–241.
[14] Z. Bao, Q. Cao, Y. Shao, S. Zhang, X. Peng, Y. Li, C. Jiang, X. Zhong, J. Wang, Carbon and oxygen-doped phosphorus nitride (COPN) for continuous selective and stable H_2O_2 production, ACS Catal. 13 (22) (2023) 14492–14502.
[15] L. Chen, Z. Yang, J. Qian, B. Pan, Interaction between organic compounds and catalyst steers the oxidation pathway and mechanism in the iron oxide-based heterogeneous fenton system, Environ. Sci. Technol. 56 (19) (2022) 14059–14068.
[16] S. Zhang, T. Hedtke, Q. Zhu, M. Sun, S. Weon, Y. Zhao, E. Stavitski, M. Elimelech, J. H. Kim, Membrane-Confined Iron Oxychloride Nanocatalysts for Highly Efficient Heterogeneous Fenton Water Treatment, Environ. Sci. Technol. 55 (13) (2021) 9266–9275.
[17] Y. Zhang, J. Tao, Y. Hu, G. Huang, Y. Pan, W. Li, J. Chen, H. Yu, Metal oxyhalide-based heterogeneous catalytic water purification with ultralow H_2O_2 consumption, Nat. Water 2 (2024) 770–781.
[18] Y. Sun, L. Han, P. Strasser, A comparative perspective of electrochemical and photochemical approaches for catalytic H_2O_2 production, Chem. Soc. Rev. 49 (18) (2020) 6605–6631.
[19] D. Li, C. Li, L. Zhang, H. Li, L. Zhu, D. Yang, Q. Fang, S. Qiu, X. Yao, Metal-Free Thiophene-Sulfur Covalent Organic Frameworks: Precise and Controllable Synthesis of Catalytic Active Sites for Oxygen Reduction, J. Am. Chem. Soc. 142 (18) (2020) 8104–8108.
[20] M.D. Simić, T.P. Brdarić, B.G.S. Rosić, Ľ. Švorc, D.J. Relić, D.D. Aćimović, Degradation of Bisphenol A *via* the electro–Fenton process using nanostructured carbon-metal oxide anodes: Intermediates and reaction mechanisms study, J. Environ. Chem. Eng. 12 (5) (2024) 113369.
[21] C. Zhang, M. Ye, H. Li, Z. Liu, Z. Fu, H. Zhang, G. Wang, Y. Zhang, Fe/Fe3C nanoparticles embedded in N-doped porous carbon as the heterogeneous electro-Fenton catalyst for efficient degradation of Bisphenol A, Sep. Purif. Technol. 316 (1) (2023) 123778.
[22] Y. Yao, J. Yang, C. Zhu, L. Lu, Q. Fang, C. Xu, Z. He, S. Song, Y. Shen, Unveiling the metallic size effect on O_2 adsorption and activation for enhanced electro-Fenton degradation of aromatic compounds, J. Hazard. Mater. 462 (15) (2023) 132739.
[23] W. Zhang, T.T. Le, D. Shin, S. Nandy, J.W. Choi, S.Y. Paek, C. Hwang, J.H. Kim, H. Suh, H. K. Chae, S.Y. Lee, S.S. Han, H. S. Kim, J.M. Kim, Higher-valent nickel oxides with enhanced two-electron oxygen reduction in advanced electro-Fenton system for organic pollutants degradation, Appl. Catal. B-Environ. Energy 361 (2024) 124666.
[24] D. Li, T. Zheng, Y. Liu, D. Hou, K.K. Yao, W. Zhang, H. Song, H. He, W. Shi, L. Wang, J. Ma, A novel Electro-Fenton process characterized by aeration from inside a graphite felt electrode with enhanced electrogeneration of H_2O_2 and cycle of Fe^{3+}/Fe^{2+}, J. Hazard. Mater. 396 (5) (2020) 122591.
[25] Z. Yang, J. Qian, A. Yu, B. Pan, Singlet oxygen mediated iron-based Fenton-like catalysis under nanoconfinement, P. Natl. Acad. Sci. USA 116 (14) (2019) 6659–6664.
[26] L. Xie, X. Liu, J. Chang, C. Zhang, Y. Li, H. Zhang, S. Zhan, W. Hu, Enhanced redox activity and oxygen vacancies of perovskite triggered by copper incorporation for the improvement of electro-Fenton activity, Chem. Eng. J. 428 (15) (2021) 131352.
[27] J. Wang, S. Li, Q. Qin, C. Peng, Sustainable and feasible reagent-free electro-Fenton *via* sequential dual-cathode electrocatalysis, P. Natl. Acad. Sci. Usa. 118 (34) (2021) e2108573118.

[28] E. Jung, H. Shin, B.H. Lee, V. Efremov, S. Lee, H.S. Lee, J. Kim, W.H. Antink, S. Park, K.S. Lee, S.P. Cho, J.S. Yoo, Y.E. Sung, Atomic-level tuning of Co–N–C catalyst for high-performance electrochemical H_2O_2 production, Nat. Mater. 19 (2020) 436–442.

[29] Y. Li, J. Chen, Y. Ji, Z. Zhao, W. Cui, X. Sang, Y. Cheng, B. Yang, Z. Li, Q. Zhang, L. Lei, Z. Wen, L. Dai, Y. Hou, Single-atom Iron Catalyst with Biomimetic Active Center to Accelerate Proton Spillover for Medical-level Electrosynthesis of H_2O_2 Disinfectant, Angew. Chem. Int. Ed. 62 (34) (2023) e202306491.

[30] K. Yu, S. Guan, W. Zhang, W. Zhang, Y. Meng, H. Lin, Q. Gao, Engineering Asymmetric Electronic Structure of Co-N-C Single-Atomic Sites toward Excellent Electrochemical H_2O_2 Production and Biomass Upgrading, Angew. Chem. Int. Ed. 64 (19) (2025) e202502383.

[31] D. Deng, J. Qian, X. Liu, H. Li, D. Su, H. Li, H. Li, L. Xu, Non-Covalent Interaction of Atomically Dispersed Cu and Zn Pair Sites for Efficient Oxygen Reduction Reaction, Adv. Funct. Mater. 32 (32) (2022) 2203471.

[32] L. Yang, H. Cheng, H. Li, G. Sun, S. Liu, T. Ma, L. Zhang, Atomic Confinement Empowered CoZn Dual-Single-Atom Nanotubes for H_2O_2 Production in Sequential Dual-Cathode Electro-Fenton Process, Adv. Mater. 36 (44) (2024) 2406957.

[33] X. Zhou, Y. Min, C. Zhao, C. Chen, M. Ke, S. Xu, J. Chen, Y. Wu, H. Yu, Constructing sulfur and oxygen super-coordinated main-group electrocatalysts for selective and cumulative H_2O_2 production, Nat. Commun. 15 (2024) 193.

[34] K. Sun, Y. Huang, Q. Wang, W. Zhao, X. Zheng, J. Jiang, H. Jiang, Manipulating the Spin State of Co Sites in Metal–Organic Frameworks for Boosting CO_2 Photoreduction, J. Am. Chem. Soc. 146 (5) (2024) 3241–3249.

[35] Y. Li, H. Sun, L. Ren, K. Sun, L. Gao, X. Jin, Q. Xu, W. Liu, X. Sun, Asymmetric Coordination Regulating D-Orbital Spin-Electron Filling in Single-Atom Iron Catalyst for Efficient Oxygen Reduction, Angew. Chem. Int. Ed. 63 (28) (2024) e202405334.

[36] Q. Li, Z. Ma, M. Liu, Y. Jiang, M. Fu, Y. Fan, X. Qin, A. Song, G. Shao, Y. Xu, High Spin-State Modulation of Catalytic Centers by Weak Ligand Field for Promoting Sulfur Redox Reaction in Lithium-Sulfur Batteries, Angew. Chem. Int. Ed. 64 (4) (2025) e202416176.

[37] Y. Dai, B. Liu, Z. Zhang, P. Guo, C. Liu, Y. Zhang, L. Zhao, Z. Wang, Tailoring the d-Orbital Splitting Manner of Single Atomic Sites for Enhanced Oxygen Reduction, Adv. Mater. 35 (14) (2023) 2210757.

[38] Y. Zang, Y. Liu, R. Lu, Q. Yang, B. Wang, M. Zhang, Y. Mao, Z. Wang, Y. Lum, Tuning Transition Metal 3d Spin state on Single-atom Catalysts for Selective Electrochemical CO_2 Reduction, Adv. Mater. 37 (16) (2025) 2417034.

[39] Q. Zhi, R. Jiang, W. Liu, T. Sun, K. Wang, J. Jiang, Atomic CoN3S1 sites for boosting oxygen reduction reaction *via* an atomic exchange strategy, Nano Res 15 (2022) 1803–1808.

[40] K. Zhao, D. Wu, W. Wu, J. Nie, F. Geng, G. Li, H. Shi, S. Huang, H. Huang, J. Zhang, Z. Zhou, Y. Wang, S. Sun, Identifying high-spin hydroxyl-coordinated $Fe^{3+}N_4$ as the active centre for acidic oxygen reduction using molecular model catalysts, Nat. Catal. 8 (2025) 422–435.

[41] C. Zhang, Z. Kong, L. Xu, H. Yao, J. Zhou, Z. Fan, K. Chen, L. Chu, W. Xing, H. Jiang, X. Wang, C. Liu, M. Huang, Magnetic Moment Descriptor–Guided Multifunctional Co Single–Atom Catalysts Enable Wide–Temperature Uninterrupted Seawater Splitting, Adv. Mater. 37 (35) (2025) 2504476.

[42] Z. Chen, H. Niu, J. Ding, H. Liu, P.H. Chen, Y.H. Lu, R. Y. Lu, W. Zuo, L. Han, Y. Guo, S.F. Hung, Y. Zhai, Unraveling the Origin of Sulfur-Doped Fe-N-C Single-Atom Catalyst for Enhanced Oxygen Reduction Activity: Effect of Iron Spin-State Tuning, Angew. Chem. Int. Ed. 60 (48) (2021) 25404–25410.

[43] G. Yang, J. Zhu, P. Yuan, Y. Hu, G. Qu, B.A. Lu, X. Xue, H. Yin, W. Cheng, J. Cheng, W. Xu, J. Li, J. Hu, S. Mu, J.N. Zhang, Regulating Fe-spin state by atomically dispersed Mn-N in Fe-N-C catalysts with high oxygen reduction activity, Nat. Commun. 12 (2021) 1734.

[44] Z. Zhang, P. Ma, L. Luo, X. Ding, S. Zhou, J. Zeng, Regulating Spin States in Oxygen Electrocatalysis, Angew. Chem. Int. Ed. 62 (15) (2023) e202216837.

[45] Y. Zhu, C. Yang, T. Lu, Y. Gan, H. Zhao, Y. Chen, Q. Cheng, H. Yang, Engineering spin state of CoN_4-C single atom catalyst for acidic electrosynthesis of hydrogen peroxide, Nano Energy 141 (2025) 111142.

[46] Z. Zhou, S. Zhao, Z. Li, P. Wang, S. Zhan, M. Wang, Activating Oxygen *via* the 3-Electron Pathway to Hydroxyl Radical by La−O_4 Single-atom on WO_3 for Water Purification, Angew. Chem. Int. Ed. 64 (6) (2024) e202418122.

[47] H. Huang, M. Sun, S. Li, S. Zhang, Y. Lee, Z. Li, J. Fang, C. Chen, Y. Zhang, Y. Wu, Y. Che, S. Qian, W. Zhu, C. Tang, Z. Zhuang, L. Zhang, Z. Niu, Enhancing H_2O_2 Electrosynthesis at Industrial-Relevant Current in Acidic Media on Diatomic Cobalt Sites, J. Am. Chem. Soc. 146 (13) (2024) 9434–9443.

[48] Y. Wu, Y. Zhao, Q. Yuan, H. Sun, A. Wang, K. Sun, G. Waterhouse, Z. Wang, J. Wu, J. Jiang, M. Fan, Electrochemically synthesized H_2O_2 at industrial–level current densities enabled by in situ fabricated few–layer boron nanosheets, Nat. Commun. 15 (2024) 10843.

[49] Q. Wu, H. Zou, X. Mao, J. He, Y. Shi, S. Chen, X. Yan, L. Wu, C. Lang, B. Zhang, L. Song, X. Wang, A. Du, Q. Li, Y. Jia, J. Chen, X. Yao, Unveiling the dynamic active site of defective carbon-based electrocatalysts for hydrogen peroxide production, Nat. Commun. 14 (2023) 6275.

[50] T. Bao, Y. Wu, C. Tang, Y. Xi, Y. Zou, P. Shan, C. Zhang, W. Drożdż, A. Stefankiewicz, P. Yuan, C. Yu, C. Liu, Highly ordered conductive metal-organic frameworks with chemically confined polyoxometalate clusters: A dual-functional electrocatalyst for efficient H_2O_2 synthesis and biomass valorization, Adv. Mater. 37 (17) (2025) 2500399.

[51] C. Zhang, P. Shan, Y. Zou, T. Bao, X. Zhang, Z. Li, Y. Wang, C. Liu, C. Yu, Stable and high-yield hydrogen peroxide electrosynthesis from seawater, Nat. Sustain 8 (2025) 542–552.

[52] Y. Xi, Y. Xiang, C. Zhang, T. Bao, Y. Zou, J. Zou, G. Wei, L. Wang, H. Xu, C. Yu, C. Liu, Perfect is perfect: nickel prussian blue analogue as a high-efficiency electrocatalyst for hydrogen peroxide production, Angew. Chem. Int. Ed. 64 (1) (2025) e202413866.

[53] Y. Zhou, L. Xu, L. Wu, W. Zhu, T. He, H. Yang, H. Huang, T. Cheng, Y. Liu, Z. Kang, The operation active sites of O_2 reduction to H_2O_2 over ZnO, Energy Environ. Sci. 16 (8) (2023) 3526–3533.

[54] C. Zhang, L. Yuan, C. Liu, Z. Li, Y. Zou, X. Zhang, Y. Zhang, Z. Zhang, C. Wei, C. Yu, Crystal engineering enables cobalt-based Metal-Organic Frameworks as high-performance electrocatalysts for H_2O_2 production, J. Am. Chem. Soc. 145 (14) (2023) 7791–7799.

[55] G. Chen, J. Liu, Q. Li, P. Guan, X. Yu, L. Xing, J. Zhang, R. Che, A direct H_2O_2 production based on hollow porous carbon sphere-sulfur nanocrystal composites by confinement effect as oxygen reduction electrocatalysts, Nano. Res. 12 (2019) 2614–2622.

[56] S. Chen, T. Luo, K. Chen, Y. Lin, K. Fu, K. Liu, C. Cai, Q. Wang, H. Li, X. Li, J. Hu, H. Li, M. Zhu, M. Liu, Chemical Identification of catalytically active sites on oxygen-doped carbon nanosheet to decipher the high activity for electro-synthesis hydrogen peroxide, Angew. Chem. Int. Ed. 60 (30) (2021) 16607–16614.

[57] R. Gao, L. Pan, Z. Li, C. Shi, Y. Yao, X. Zhang, J. Zou, Engineering facets and oxygen vacancies over hematite single crystal for intensified electrocatalytic H_2O_2 production, Adv. Funct. Mater. 30 (24) (2020) 1910539.

[58] K. Jiang, S. Back, A.J. Akey, C. Xia, Y. Hu, W. Liang, D. Schaak, E. Stavitski, J. K. Nørskov, S. Siahrostami, H. Wang, Highly selective oxygen reduction to hydrogen peroxide on transition metal single atom coordination, Nat. Commun. 10 (2019) 3997.

[59] M. Liu, Y. Li, Z. Qi, H. Su, W. Cheng, W. Zhou, H. Zhang, X. Sun, X. Zhang, Y. Xu, Y. Jiang, Q. Liu, S. Wei, Self-nanocavity-confined halogen anions boosting the high selectivity of the two-electron oxygen reduction pathway over Ni-based MOFs, J. Phys. Chem. Lett. 12 (36) (2021) 8706–8712.

[60] X. Sun, Y. Li, H. Su, X. Zhang, Y. Xu, W. Zhou, M. liu, W. Cheng, Q. Liu, Dissecting π-conjugated covalent-coupling over conductive MOFs toward efficient two-electron oxygen reduction, Appl. Catal. B Environ. 317 (15) (2022) 121706.

[61] H. Wu, T. He, M. Dan, L. Du, N. Li, Z. Liu, Activated Ni-based Metal Organic Framework catalyst with well-defined structure for electrosynthesis of hydrogen peroxide, Chem. Eng. J. 435 (2022) 134863.

[62] J. Zhang, G. Zhang, S. Jin, Y. Zhou, Q. Ji, H. Lan, H. Liu, J. Qu, Graphitic N in nitrogen-doped carbon promotes hydrogen peroxide synthesis from electrocatalytic oxygen reduction, Carbon 163 (15) (2020) 154–161.

[63] Z. Chen, H. Niu, J. Ding, H. Liu, P. Chen, Y. Lu, Y. Lu, W. Zuo, L. Han, Y. Guo, S. Hung, Y. Zhai, Unraveling the origin of sulfur-doped Fe-N-C single-atom catalyst for enhanced oxygen reduction activity: Effect of Iron Spin-State Tuning, Angew. Chem. Int. Ed. 60 (48) (2021) 25404–25410.

[64] A. Kudlu, D. Sarma, D.K. Das, A. Sunil, T.J. Maliakal, A. Mahata, J. Kundu, Antimony dopant-driven monomer-dimer structural transition in a zero-dimensional indium halide hybrid, J. Phys. Chem. Lett. 17 (8) (2026) 2286–2295.

[65] X. Zhang, Q. Zhang, J. Cui, J. Yan, J. Liu, Y. Wu, New insights into the key bifunctional role of sulfur in Fe-N-C single-atom catalysts for ORR/OER, Nanoscale 14 (2022) 3212–3223.

[66] Y. Gu, Y. Tan, H. Tan, Y. Han, D. Cheng, F. Lin, Z. Qian, L. Zeng, S. Zhang, R. Zeng, Y. Liu, H. Guo, M. Luo, S. Guo, Industrial electrosynthesis of hydrogen peroxide over p-block metal single sites, Nat. Synth. 4 (2025) 614–621.

[67] S. Chen, T. Luo, X. Li, K. Chen, J. Fu, K. Liu, C. Cai, Q. Wang, H. Li, Y. Chen, C. Ma, L. Zhu, Y. Lu, T. Chan, M. Zhu, E. Cortés, M. Liu, Identification of the Highly Active Co–N_4 Coordination Motif for Selective Oxygen Reduction to Hydrogen Peroxide, J. Am. Chem. Soc. 144 (32) (2022) 14505–14516.

[68] C. Yang, S. Shang, L. Lin, P. Wang, Z. Ye, Y. Wang, K. Shih, L. Sun, X. Li, Electro-driven cycling Fenton catalysis through two–dimensional electroresponsive metal–organic frameworks for water purification, Nat. Water 2 (2024) 793–802.

[69] I.A. Katsoyiannis, S. Canonica, U. Gunten, Efficiency and energy requirements for the transformation of organic micropollutants by ozone, O_3/H_2O_2 and UV/H_2O_2, Water Res 45 (13) (2011) 3811–3822.

[70] M. Al-Obaidi, J. Li, S. Alsadaie, C. Kara-Zaïtri, I. Mujtaba, Modelling and optimisation of a multistage Reverse Osmosis processes with permeate reprocessing and recycling for the removal of N–nitrosodimethylamine from wastewater using Species Conserving Genetic Algorithms, Chem. Eng. J. 350 (15) (2018) 824–834.

[71] Z. Zhao, P. Wang, C. Song, T. Zhang, S. Zhan, Y. Li, Enhanced Interfacial Electron Transfer by Asymmetric Cu-O_V-In Sites on In_2O_3 for Efficient Peroxymonosulfate Activation, Angew. Chem. Int. Ed. 62 (11) (2023) e202216403.

[72] G. Kresse, J. Furthmüller, Efficiency of ab-initio total energy calculations for metals and semiconductors using a plane-wave basis set, Comput. Mater. Sci. 6 (1) (1996) 15–50.

[73] P. Blöchl, Projector augmented-wave method, Phys. Rev. B 50 (1994) 17953.

[74] J. Perdew, K. Burke, M. Ernzerhof, Generalized gradient approximation made simple, Phys. Rev. Lett. 77 (1996) 3865.

[75] J. Nørskov, J. Rossmeisl, A. Logadottir, L. Lindqvist, J. Kitchin, T. Bligaard, H. Jónsson, Origin of the overpotential for oxygen reduction at a fuel-cell cathode, J. Phys. Chem. B 108 (46) (2004) 17886–17892.